The Dissertation Committee for Joo-Yun Jung Certifies that this is the approved version of the following dissertation:

Methods to Achieve Wavelength Selectivity in Infrared Microbolometers and Reduced Thermal Mass Microbolometers

Committee:

Dean P. Neikirk, Supervisor

Seth Bank

Mikhail Belkin

Neal Hall

Robert L. Rogers

METHODS TO ACHIEVE WAVELENGTH SELECTIVITY IN INFRARED MICROBOLOMETERS AND REDUCED THERMAL MASS MICROBOLOMETERS

by

JOO-YUN JUNG, B.S.E.E.; M.S.E.E.

DISSERTATION

Presented to the Faculty of the Graduate School of
The University of Texas at Austin
in Partial Fulfillment
of the Requirements
for the Degree of

DOCTOR OF PHILOSOPHY

The University of Texas at Austin
DECEMBER 2010

Dedication

To my wife, Sunju Sohn, for love and support

Acknowledgements

It has been a long journey, and I would not even know where to begin. First and foremost I would like to thank Dr. Dean P. Neikirk, my adviser. Thank you very much for giving me many crazy ideas which inspire me to finish a long journey.

During my time at UT as a graduate student, I have been very fortunate to have had the opportunity to work with people, Team Neikirk who are outstanding individuals both personally and professionally, and I would like to thank them for their help during my time here at UT. This group has almost always been a lot of fun, and has almost always been supportive of my efforts. Within this group I must extend special thanks to Jong Yeon Park, Praveenkumar Pasupathy, Ye Chen, and Sheng Zhang. Aslo, I would like to acknowledge Aniruddha S. Weling who measured a number of fabricated devices. I also must show my appreciation to the past members of Team Neikirk: Jooyong Kim, Byungki Woo, Junwan Kim, Sangwook Han, and Yoonsuk Park.

I wish to thank the members of my committee; Dr. Seth Bank, Dr. Mikhail Belkin, Dr. Neal Hall, and Dr. Robert L. Rogers, for their patience and support and would like to commend them for their inspirational teaching and excellence in their respective fields.

I would like to thank my parents, Chang-Sik Jung and Kyung-suk Park, for their continued enthusiastic support of my education, and parents-in-law, Jin-Hun Sohn and Sook-Hee Kim for their encouragement and support. I want to let my son and daughters, Tory, Hannah, and Byuri know that I love them dearly. I would finally like to thank my wife Sunju Sohn whose support, love, and help made much of this work possible. Her encouragement to me has always been invaluable.

METHODS TO ACHIEVE WAVELENGTH SELECTIVITY IN INFRARED MICROBOLOMETERS AND REDUCED THERMAL MASS MICROBOLOMETERS

Publication No._____________

Joo-Yun Jung, Ph.D.
The University of Texas at Austin, 2010

Supervisor: Dean Paul Neikirk

The use of a patterned resistive sheet as an infrared-selective absorber, including the effects of a mechanical support dielectric layer is discussed. Also, modified dielectric coated Salisbury Screen can improve both the wavelength selectivity and the speed of thermal response for microbolometers. These patterned resistive sheets and Modified dielectric coated Salisbury Screen are a modified form of classical Salisbury Screens that utilize a resistive absorber layer placed a quarter-wavelength in front of a mirror. These structures can show a narrower detection bandwidth when compared to conventional microbolometers. For a Modified dielectric coated Salisbury Screen for multi-spectral system, wavelength selectivity can be varied by changing the distance to the mirror, and for patterned resistive sheet, wavelength selectivity can be varied by changing the lithographically drawn parameters of the array. Hence, different pixels in a focal plane array can be designed to produce a "multi-color" infrared imaging system. Also, the thermal mass of microbolometer is reduced using patterned resistive structure.

Table of Contents

List of Tables

List of Figures

Chapter 1: Introduction

1.1 CONVENTIONAL MICROBOLOMETERS

Bolometer is a temperature sensitive resistor that operates based on the temperature rise caused by absorption of the incident infrared radiation. When bolometer is much smaller than the wavelength, it is called microbolometers. The definition of microbolometers, however, has been used more in general, such as physically small bolometers also being called as microbolometers.

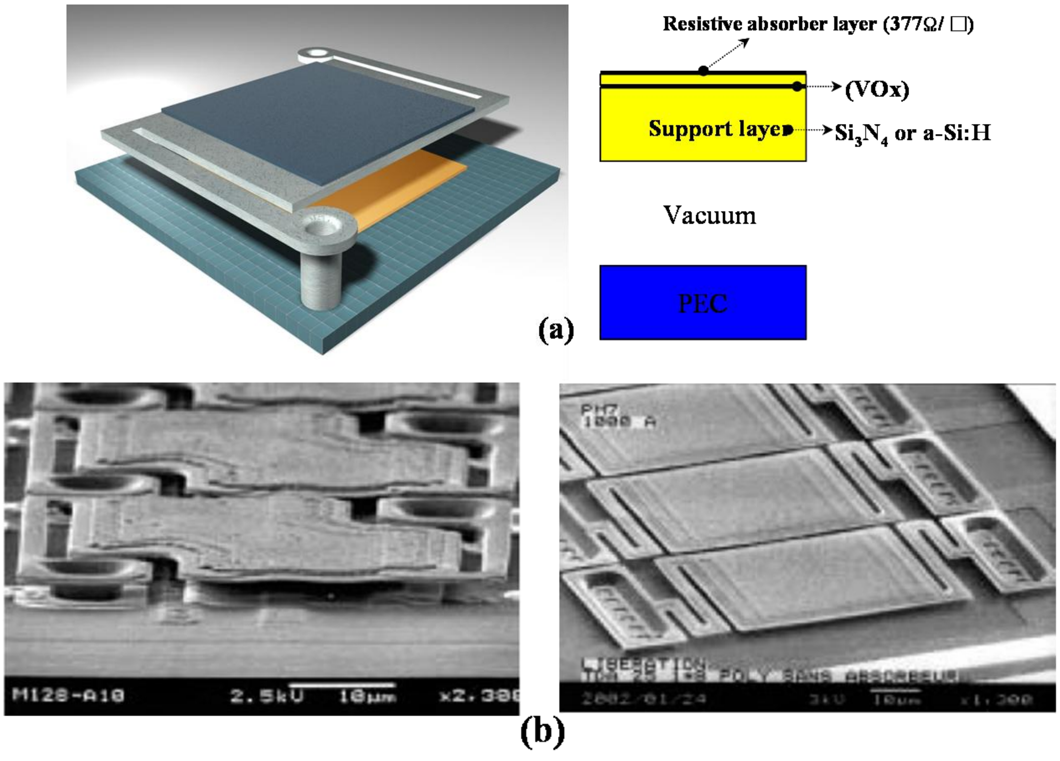

Figure 1.1: (a) Configuration of conventional microbolometers; (b) pixel of conventional microbolometer [1].

Figure 1.1 shows configuration of a basic microbolometer called Salisbury Screen. Salisbury Screen was first introduced as an electromagnetic absorber during World War II and has been used as broad band electromagnetic absorbers. It consists of resistive layer placed quarter-wavelength in front of mirror layer. There is also a mechanical support layer below the resistive layer for fabrication issue and long support arms for sensitive response requiring high thermal resistance. There are two main streams of conventional microbolometers. One is vanadium oxide (VOx) microbolometer [2], and other is amorphous silicon (a-Si) microbolometer [3, 4]. Vanadium oxide microbolometer uses silicon nitride as a support layer and absorber layer. A resistive sheet layer with sheet resistance $R_s = 377\Omega/\square$ can also be used as an additional absorber layer.

Amorphous silicon microbolometer uses a-Si as a support layer and bolometric layer. Resistive sheet layer with sheet resistance $R_s = 377\Omega/\square$ is the absorber layer in this microbolometer. By changing the design parameters such as sheet resistance of resistive sheet layer and air gap thickness, it is possible to tailor the device spectral responses. Power absorption efficiency is normalized power absorption by the resistive sheet layer. It is 1 – reflected power. The most used wavelength band is between 7 and 14um long infrared region. Figure 1.2 shows the spectral responses of power absorption efficiency of Salisbury Screen. It shows broad absorption through LWIR band. However, its bandwidth is too broad to construct wavelength selectivity in LWIR band. Therefore, this dissertation research focused on constructing new designs with narrow bandwidth that enhanced wavelength selectivity. More information is provided in the following chapters.

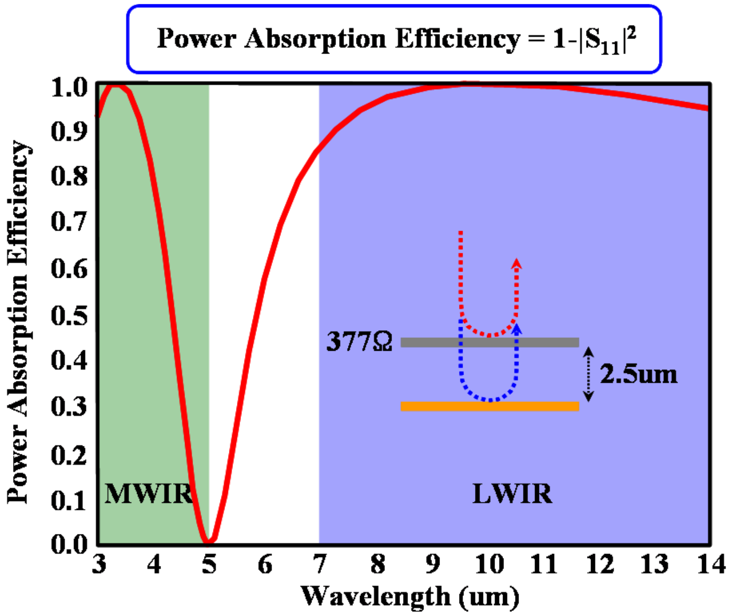

Figure 1.2: the spectral response of Salisbury Screen with sheet resistance R_s = 377Ω/□ of resistive sheet layer and air gap distance d = 2.5μm.

1.2: MULTI-SPECTRAL MICROBOLOMETERS

Multi-spectral infrared detection has been an interest, as the detection permits rapid and efficient understanding in a variety ways [5]. For example, discrimination of both absolute temperature and unique spectral signatures of objects in the scene is possible so as to subtract spurious information leaving only the objects of interest. Therefore, multi-spectral, wavelength selective infrared detection has been extensively studied for numerous military and commercial applications, e.g., target acquisition, battlefield assessment, missile guidance and defense, surveillance, night vision, thermal imaging, nondestructive detection, medical diagnostics, remote sensing, and so on. Additionally, the 7 to 14μm infrared band of the electromagnetic spectrum is known as the “fingerprint” region since it exhibits an abundance of molecular resonances – vibration, rotational, and low-lying electronic transitions so that it provides highly detailed and precise information. Consequently, the multi-spectral infrared detection of 7 to 14μm infrared band can give various information that single-spectral infrared detection can not give. Figure 1.3 is an example of single- and multi-spectral infrared detection at a basaltic crater of Mars taken by NASA [6]. The top in Fig. 1.3 at the top is single-spectral infrared detection, a grayscale image showing only surface temperature, whereas Fig. 1.3 at the bottom is multi-spectral infrared detection, a false-color composite made from three individual infrared bands showing the composition of the crater. According to NASA, this image is particularly useful because there appears to be more than one type of sand at the bottom of this crater and in the hummocky terrain near the bottom of the image. The pink/magenta areas are characteristics of a basaltic composition, but there are also orange areas that are likely caused by the presence of andesite. These two compositions, basalt and andesite, are some of the most common found on Mars. As such, multi-spectral infrared detection makes this detailed inspection possible, while single-spectral infrared detection can only provide the information on temperature.

In order to construct a multi-spectral microbolometer, microbolometer has to produce the wavelength-selective narrowband absorption in LWIR band. In 1960's, metal mesh grid was used as a frequency-selective filter [7, 8]. The inductive metal mesh grid, which consists of highly conducting metal sheet (assuming perfect conducting sheet) with periodic square slots, was used as band pass filter or high pass filter. Also, since 1970's, frequency selective surfaces (FSS), which have periodic pattern on metal or dielectric layer, has been used as a filter [9-11]. These frequency selective surfaces with periodic rectangular and cross pattern slots can produce narrowband transmission. Recently, metamaterial absorber has become popular, which consists of periodic metallic small structure or pattern that produces wavelength-selective narrowband absorption [12,13].

Finally, the quarter-wave distributed Bragg reflector (DBR) has been applied to produce the wavelength-selective narrowband absorption [14].

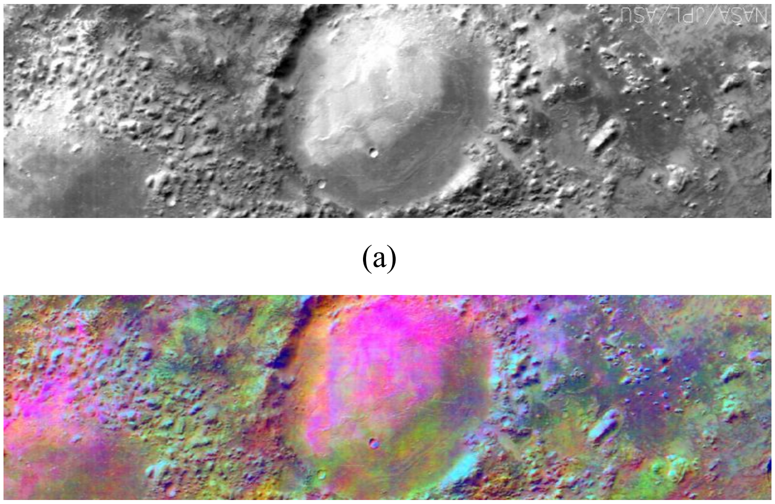

(a)

(b)

Figure 1.3: Two representations of the same infrared image of a basaltic crater near Nili Fosse in the the Isidis region of Mars. The top is single-spectral infrared detection, a grayscale image showing surface temperature, and the bottom is multi-spectral infrared detection, a false-color composite made from 3 individual bands [6].

Chapter 2: Dielectric Coated Salisbury Screen

Using a simple Salisbury Screen makes it difficult to achieve narrow band absorption. To allow ourselves more design freedom and to produce wavelength selectivity, we add a dielectric coating to the resistive absorber layer. Another method that allows for wavelength selectivity is to use, as shown in Fig. 2.1, a dielectric-coated Salisbury Screen. The screen consists of a resistive layer coated on both sides with transparent dielectric layers, all placed in front of a mirror.

2.1 DIELECTRIC COATED SALISBURY SCREEN (DSS)

The Salisbury Screen consists of a resistive absorber layer ($377\Omega/\square$) placed a quarter-wavelength in front of mirror. To fabricate this structure, there should be a mechanical support dielectric layer. The Salisbury Screen cannot, however, produce a narrow band spectral response in the long wave infrared (LWIR) band. To achieve greater design freedom and to produce wavelength selectivity in the narrow band, we coat the resistive sheet layer, shown in Fig. 2.1, with a dielectric layer. Without multiple interferences caused by the dielectric layers, a resistive sheet and mirror cannot generate narrow band absorption. I along with my colleague Sangwook Han tried to use Si_3N_4 as the dielectric layer. Si_3N_4 is a well-known structural material in MEMS and, for our group, easily accessible. Due to its high absorption and dispersion in LWIR, Si_3N_4 was not an appropriate material for narrow band application.

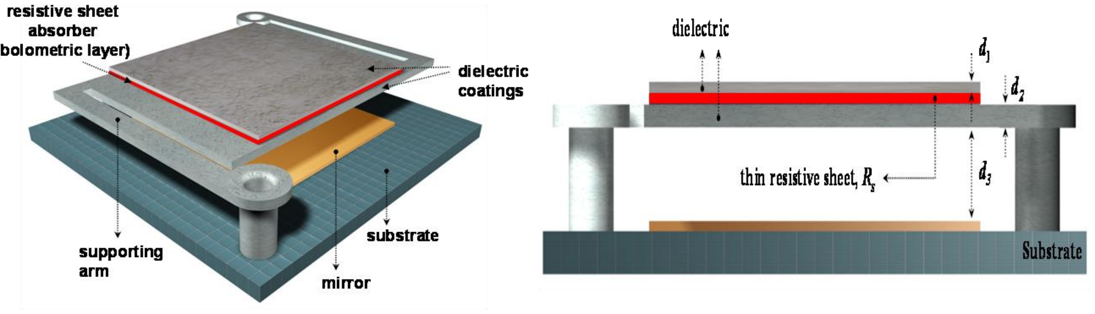

Figure 2.1: Configuration of dielectric coated Salisbury Screen (DSS) and design parameters.

Germanium (Ge), in contrast, is almost lossless in LWIR [15], and was selected for as the dielectric layer. To find the proper thickness of the Ge support layers, we used a Genetic Algorithm (GA) as an optimization scheme. To locate narrow bandwidth array designs that couple strongly at a desired wavelength, we used a cost definition for the GA. It seeks high power absorption at a specified wavelength and seeks low power absorption at other wavelengths. This is accomplished by minimizing the area under the absorption curve, as given by:

$$\begin{cases} \text{if } \mathrm{PAE}\big|_{\text{desired}\,\lambda} > \mathit{threshold}, & \mathit{cost} = \int_{7\mu m}^{14\mu m} \mathrm{PAE}(\lambda)\; d\lambda \\ \qquad \text{otherwise}, & \mathit{cost} = \infty \end{cases} \qquad \text{Eq. 2.1}$$

where PAE stands for power absorption efficiency. Figure 2.2 shows the results of a GA design for three colors centered at 8, 10, and 12 µm. The GA results indicate that in each case the air gap is approximately half the center wavelength; i.e., $d_3 \approx \lambda_c/2$. An examination of the dielectric-layer thicknesses suggests that the dielectric layer below the absorber should be a quarter dielectric wavelength thick; i.e., $d_2 \approx (\lambda_c/n)/4$ (where n is the index of refraction of the dielectric), and the dielectric layer above the absorber should be either a half or full dielectric wavelength thick; i.e., $d_1 \approx (\lambda_c/n)/2$

or $d_1 \approx (\lambda_c/n)$. These general design rules are illustrated in Fig. 2.3. Using these guidelines should simplify designing a dielectric-coated Salisbury screen (DSS) with any desired center wavelength. From the perspective of microbolometer speed performance, there is a trade-off between the two choices for the dielectric layer above the absorber. The GA-optimized designs indicate that for best spectral performance this layer should be either a half or full dielectric wavelength thick; i.e., $d_1 \approx (\lambda_c/n)/2$ or $d_1 \approx (\lambda_c/n)$. The thicker choice ($d_1 \approx (\lambda_c/n)$), however, would increase the thermal mass of the microbolometer and lead to slower response. Figure 2.4 illustrates the difference in spectral responses for the two designs with the same center wavelength of 10 µm. The GA-optimizer selected the thicker top layer $d_1 \approx (\lambda_c/n)$, thus giving the higher thermal mass (slower) design. If we compare the response of the thicker top layer to that of the thinner, it is apparent that the central peaks are nearly identical, but for the thinner top layer the shorter wavelength side peak is closer to the central peak. This may or may not, depending on the specific application, be acceptable.

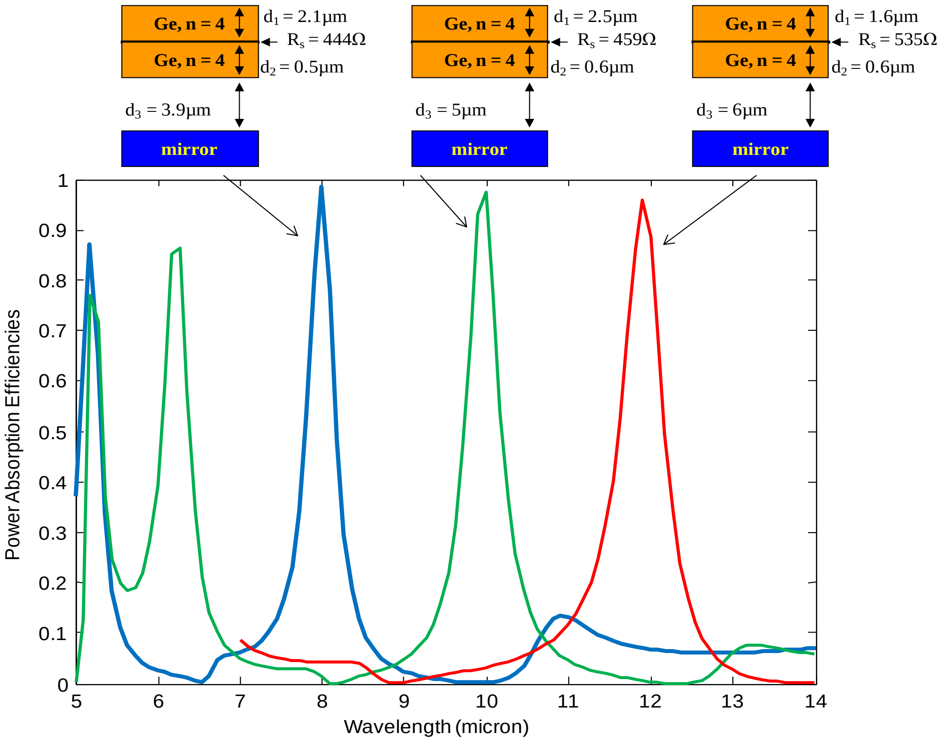

Figure 2.2: GA-optimized design for a three IR color array of dielectric coated Salisbury Screens including air gap.

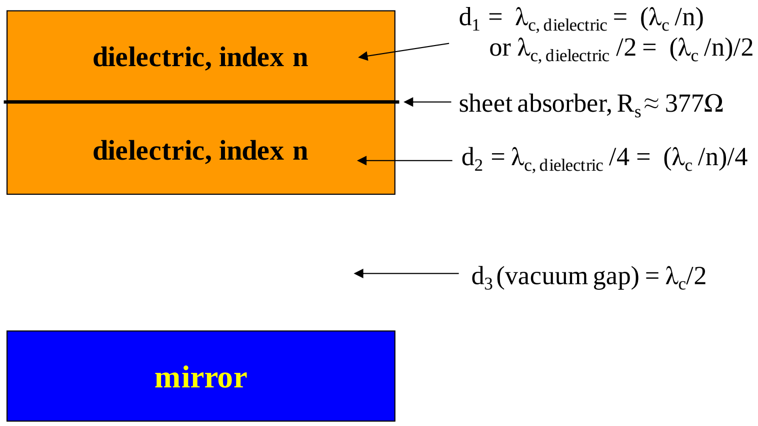

Figure 2.3: General design approach for a dielectric coated Salisbury Screen including air gap, where λ_c is the desired center wavelength, and *n* is the index of refraction of the dielectric.

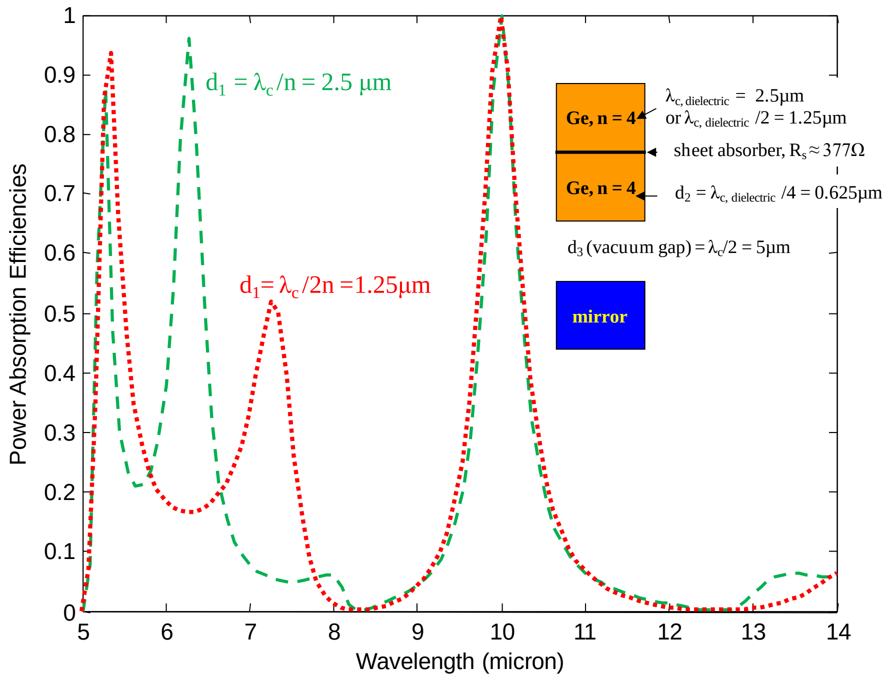

Figure 2.4: Comparison of two top layer coatings with different thicknesses for a dielectric coated Salisbury Screen.

2.2 MODIFIED DIELECTRIC COATED SALISBURY SCREEN

I have now finalized the basic design of our wavelength-selective Salisbury screen microbolometer. In achieving wavelength selectivity, the structure makes use of low loss dielectric layers to produce desirable interference effects. I have now shown that our previous design using a dielectric layer both above and below the absorbing sheet provides little advantage over a new, lower thermal mass structure with only a dielectric layer below the absorber, seen in Fig. 2.5.

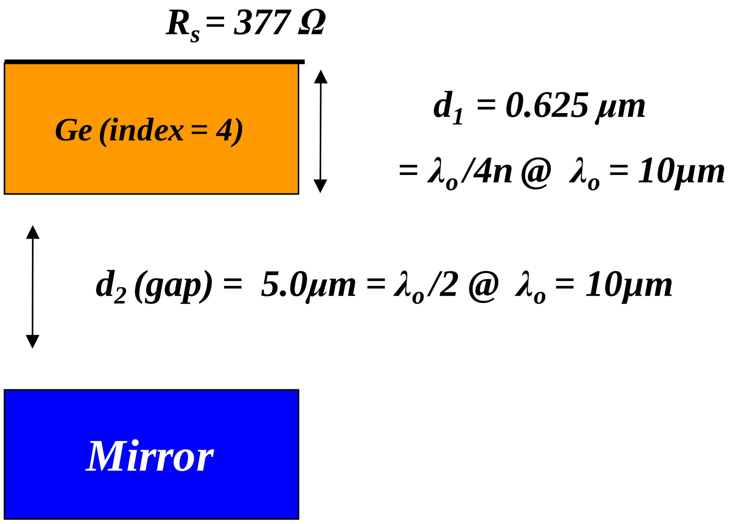

Figure 2.5: Basic design of a wavelength-selective modified dielectric coated Salisbury Screen.

Figure 2.6 shows a dielectric layer both above and below the absorbing sheet; it produces a slightly narrower band than the lower thermal mass structure with only a dielectric layer below the absorber. The central peaks are nearly identical. When the dielectric layer is both above and below the absorbing sheet, however, its shorter wavelength side peak is closer to the central peak. In microbolometer applications, we increase the speed of thermal response by reducing the thermal mass. Hence for a microbolometer it is much better to have a lower thermal mass structure with only a dielectric layer below the absorber.

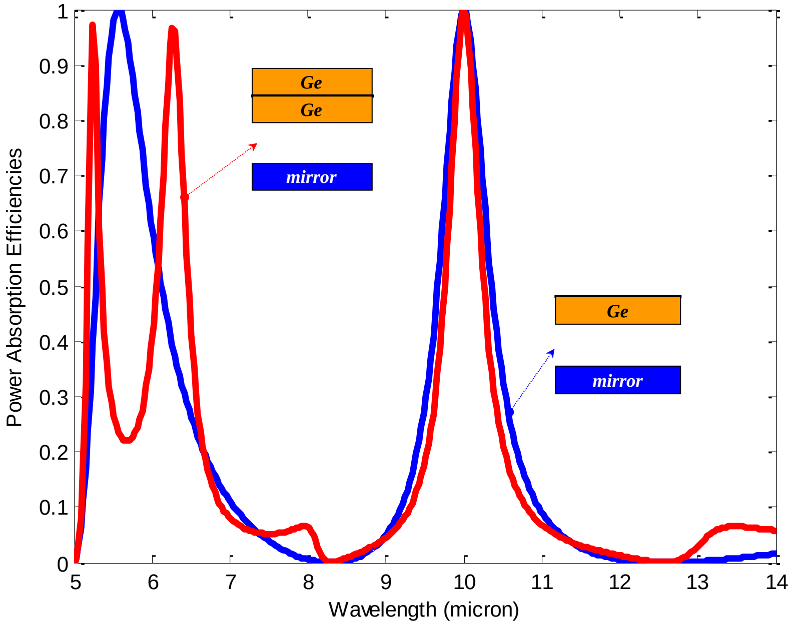

Figure 2.6: A comparison of calculated absorption spectral responses for a wavelength-selective Salisbury screen using dielectric layers both above and below the absorbing sheet (red curve) and a lower thermal mass structure with only a dielectric layer below the absorber (blue curve).

Also, this structure is air gap tunable; i.e., by varying only the air gap, we shift (tune) the center wavelength, as shown in Fig. 2.7.

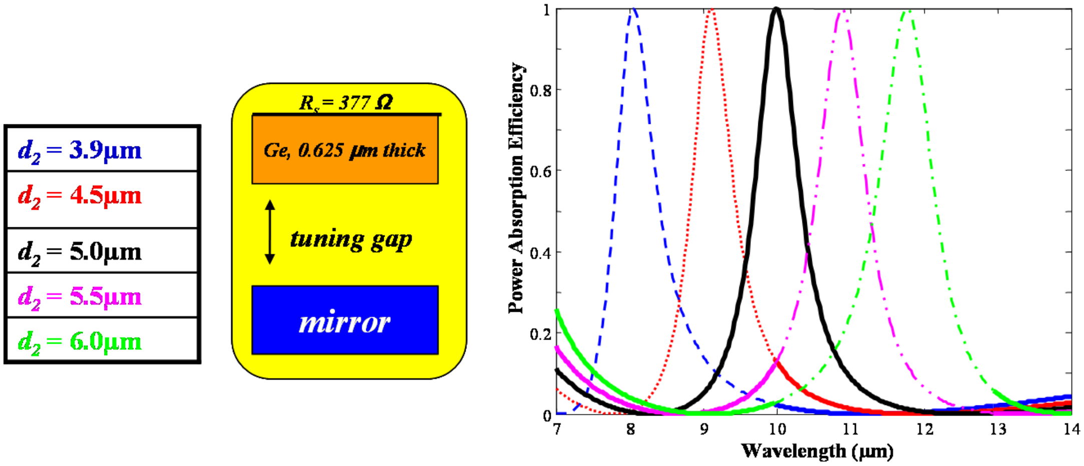

Figure 2.7: Calculated absorption spectral responses for air-gap-tunable lower thermal mass structure with only a dielectric layer below the absorber; the peaks of absorption curves are: at wavelength 10μm when air gap thickness d_2 = 5.0μm (black solid curve), at wavelength 8μm when air gap thickness d_2 = 3.9μm (blue dashed), at wavelength 9μm when air gap thickness d_2 = 4.5μm (red dotted), at wavelength 11μm when air gap thickness d_2 = 5.5μm (magenta dashed-dotted-dotted), at wavelength 12μm when air gap thickness d_2 = 6.0μm (green dashed-dotted).

2.3 FABRICATION OF MODIFIED DIELECTRIC COATED SALISBURY SCREEN

The first step in the fabrication process starts with the depositing of aluminum (0.15μm) as a reflective mirror on a silicon substrate. Next a controlled-thickness polyimide layer is spin-coated and cured, followed by a photolithography step and, to define a polyimide pattern, an etch step. We follow these steps by depositing a controlled-thickness Ge structural layer using evaporation on polyimide sacrificial layer, patterning and etching the Ge structural layer, and then removing the polyimide sacrificial layer by using an oxygen plasma asher. Finally, we deposit the resistive absorber layer using chromium (Cr) with the appropriate sheet resistance.

To fabricate a free-standing structure such as a micro bridge structure, we should include the sacrificial layer. Several sacrificial layers are commonly used in MEMS fabrication, including silicon dioxide, polysilicon, and polyimide. Polyimide, which can be removed by oxygen plasma ashing process [16], is used for device fabrication. Since the polyimide can be applied by spin coating, it can provide some surface planarization for the silicon circuitry beneath; after curing, polyimide is stable at the temperatures involved in the later processing steps. In device fabrication, layers of PI-2610 and PI-2611 polyimide (HD Microsystems) are used as sacrificial layers. Figure 2.8 shows the optimal curing process for producing polyimide 2610 and 2611 spacer layers. After the curing process, the polyimide is then patterned using photolithography and dry etch with oxygen plasma. Figure 2.9 shows the results of polyimide etch rate for PI-2610 and PI-2611 respectively.

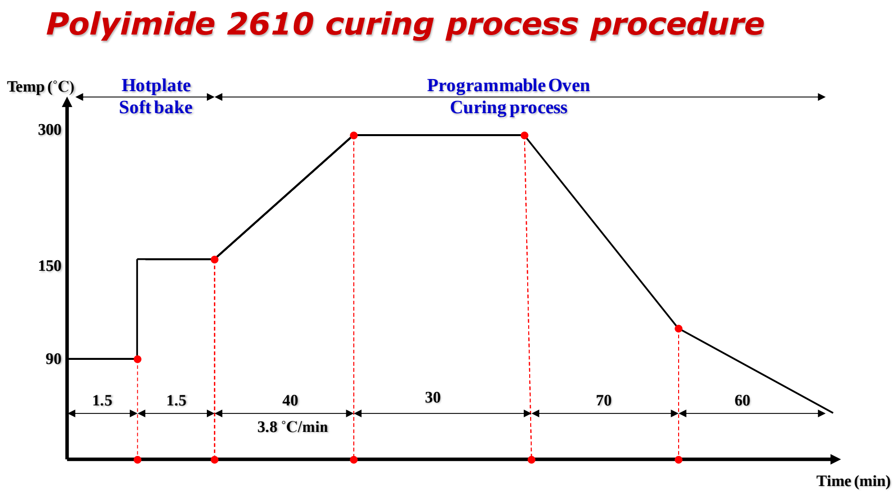

Figure 2.8: Depiction of the curing process used to produce polyimide spacer layers.

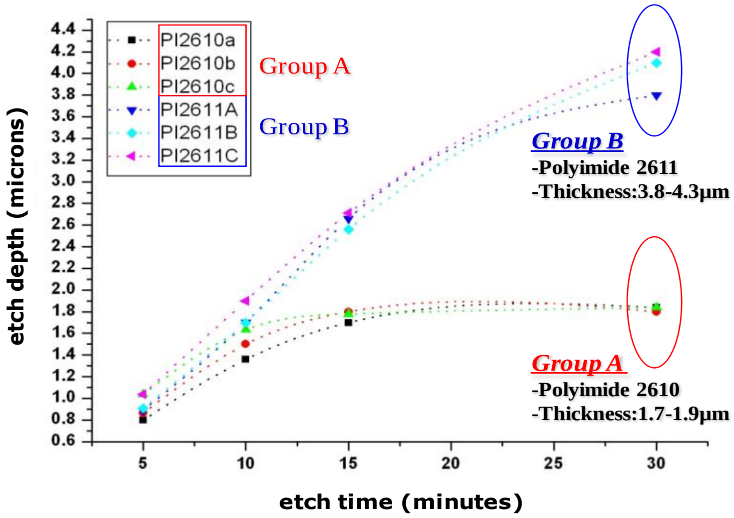

Figure 2.9: Results of polyimide etch rate for two thicknesses of polyimide using dry oxygen plasma etching.

What follows are the process steps used to pattern the Ge layer and remove the polyimide. First, the PI-2611 polyimide sacrificial layer is coated and the designed thickness of the sacrificial layer is obtained. Second, the Ge structure is deposited using an e-bema evaporator; the Ge deposition rate in the e-beam evaporator is 1.5 Å/S. Third, the Ge etch rate in RIE for plasma produced by 50 sccm CF4 gas flow rate and RF power 150W is 0.1um/min. Finally, the sacrificial layer is removed by using an oxygen plasma asher. The polyimide ashing rate in the oxygen plasma asher for plasma produced by 100 sccm oxygen flow rate and RF power 300W at chamber pressure of 1000mTorr is 0.34um/min. Two different pixel size structures were fabricated: 50 µm x 50 µm and 150 µm x 150 µm. A scanning electron micrograph and a microscope micrograph of the modified dielectric coated Salisbury Screen devices, shown in Fig. 2.10, show that after removing the sacrificial layer the germanium layer is smooth and flat. Due to the thicker sacrificial layer (about 5µm), when the Ge structure layer is patterned using a photolithography, a thicker photoresist is required for good step coverage. Sometimes, however, an undeveloped residual photoresist around the edge of the polyimide causes some residual Ge, as shown in Fig. 2.10 (d), to form around the structure.

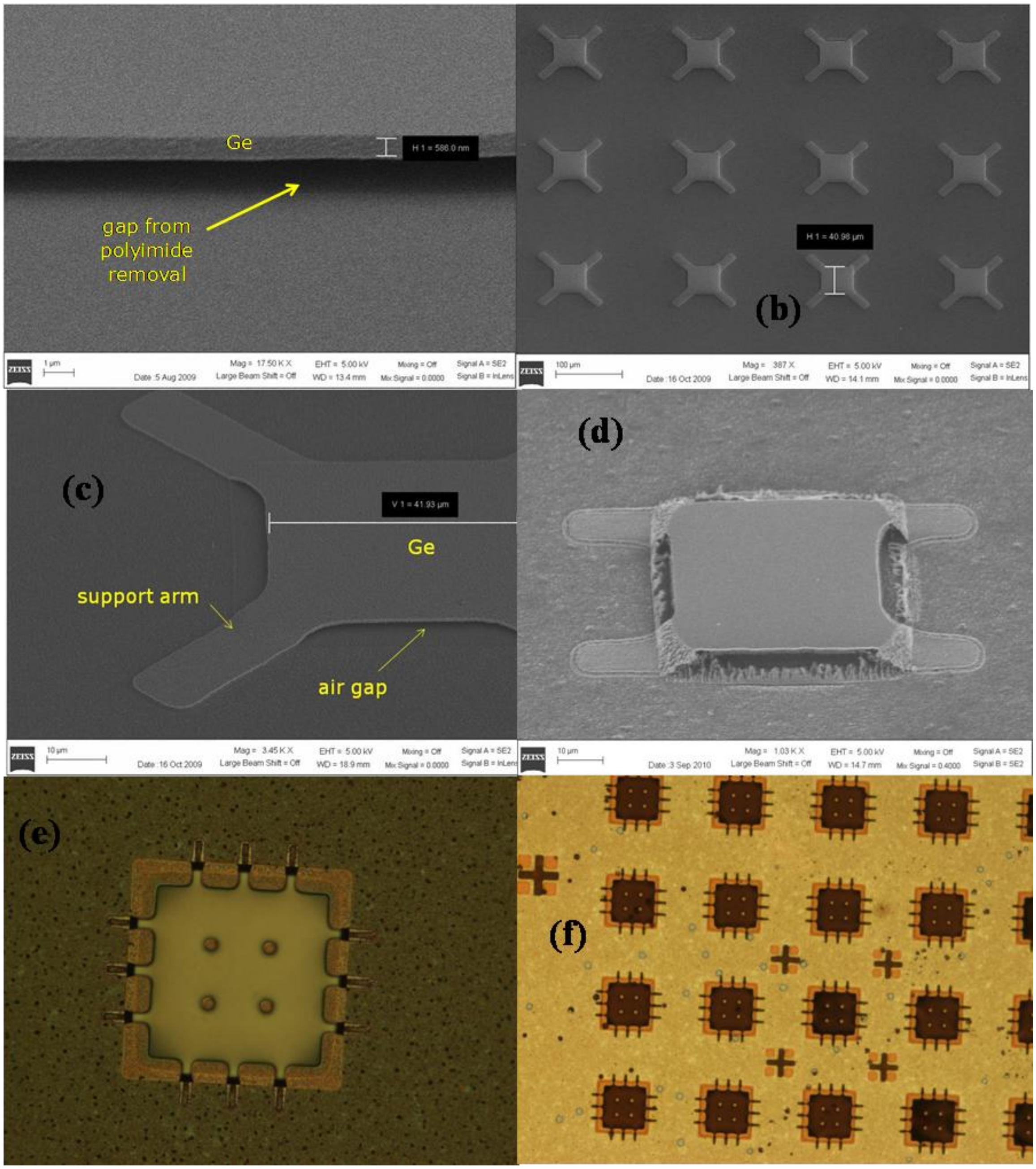

Figure 2.10: (a) SEM of Ge structure layer after polyimide undercut using an oxygen plasma ashing process, (b) SEM of modified DSS structure showing the X-shaped support arms, (c) SEM of modified DSS structure showing the X-shaped support arms and the air gap formed under the Ge structure layer, (d) SEM of residual Ge around H-shaped structure, (e) and (f) Microscope micrograph of 150 µm x 150 µm size single pixel with 4 ashing holes.

2.4 MEASUREMENT AND RESULTS

To characterize the spectral responses of the finished modified DSS devices, FTIR microscope measurements were taken on a number of the fabricated devices. All FTIR-microscope-measured data were done by Ani Weling (Foster-Miller). Measurements were taken with a Digilab FTIR (Model FTS-7000) microscope in reflectance mode at 4 cm^{-1} resolution. The reference spectra in each case were recorded on the Cr-Al mirror in an equivalent area right next to the sampled area. The cooled MCT detector with the KBr beamsplitter goes out to ~700 cm^{-1} (i.e., 14 um) and is 250 X 250 um in size. The high NA microscope system allows an adjustable field of view up to the detector size; tests were done on two different pixel sizes of each device using 70 µm x 70 µm and 30 µm x 30 µm field sizes. The FTIR spectral responses for both field sizes were essentially the same.

To determine if the measured spectral response of the fabricated modified DSS pixels match our EM models, we made a number of calculations. Germanium is supposed to be a lossless dielectric in the LWIR band [15].Since the e-bema evaporator is open to any material, however, the germanium may include impurities. Impurities would cause Ge to be lossy in the LWIR band, during the depositing of Ge using the e-beam evaporator. To more accurately model the germanium layer, I have included finite loss, using a frequency independent value for ε" obtained by fitting the FTIR measurements of a single germanium layer on an Al mirror, as shown in Fig. 2.11.

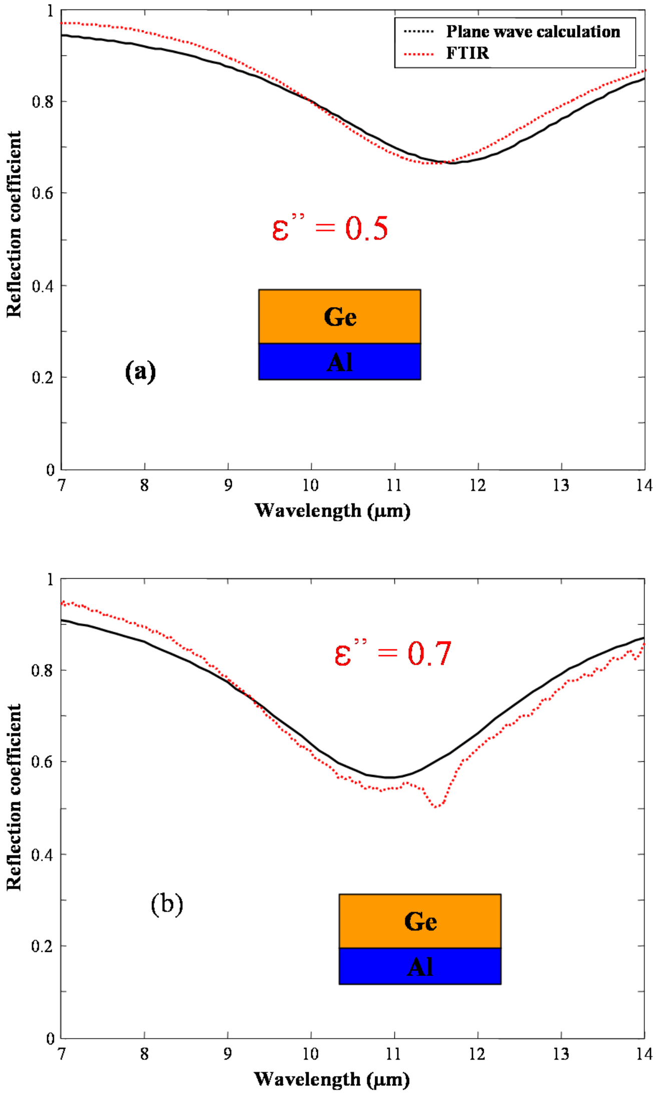

Figure 2.11: Measured FTIR and fitted spectral response for e-beam evaporated Ge layer on an aluminum mirror; (a) measured data (red curve) and plane wave calculation (black) for Ge layer deposited in October 2009; (b) measured data (red curve) and plane wave calculation (black) for germanium layer deposited in July 2010.

For this structure the designed thickness of Ge is 0.6µm, which is shown by the crystal thickness monitor of the evaporator. The optical thickness of Ge, however, is about 0.7µm; this obtains a good fit for ε” if we assume the index of refraction for Ge is 4 [15]. When germanium was deposited in October of 2009, Figure 2.11 (a) shows a good fit for ε” = 0.5. Also, the germanium deposited in July of 2010 has ε” = 0.7; this obtains a good fit with measurement data as shown in Fig. 2.11 (b). The modified DSS without resistive absorber layer was measured to determine ε” of Ge.

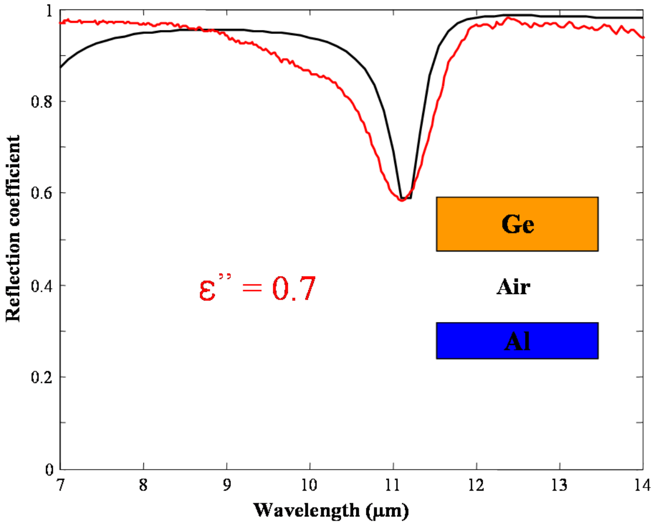

Figure 2.12: Measured FTIR and fitted spectral response for modified DSS without resistive absorber layer; measured data (red curve) and plane wave calculation (black curve) for germanium layer deposited in July 2010.

The plane wave calculation (black curve) for the modified DSS without resistive absorber layer, which has a thickness of Ge d_1 = 0.7µm, finite loss ε” = 0.7, and air gap thickness d_2 = 5.6µm, agrees with FTIR measured data (red curve).

As mentioned above, to produce the maximum power absorption, the resistive absorber layers of the Salisbury Screen and the modified DSS need to have sheet resistance R_s = 377Ω/□. We can obtain a thin resistive absorber layer by controlling the thickness of a high resistivity metal, such as chromium (Cr) or tantalum nitride (TaN). We measured the dc sheet resistance of a thin metallic absorber layer using a four-point probe. Cr films eighteen nanometers thick yield a dc sheet resistance of R_s = 400Ω/□. It is assumed that a metallic absorber layer with high dc sheet resistance has, in the LWIR band, the same high sheet resistance. Figure 2.13 compares the measured FTIR microscope absorption data (red curve) for a germanium-layered Salisbury Screen with a Cr absorber layer (R_s = 400Ω/□). It also shows the plane wave calculations for a germanium-layered Salisbury Screen with three different sheet resistances. The plane wave calculation with dc sheet resistance R_s = 400Ω/□ (black curve) agrees well with the FTIR microscope measurement (red curve). The sheet resistance R_s = 400Ω/□ of Cr absorber layer in the LWIR band behaves as the dc sheet resistance R_s = 400Ω/□, which is measured with a four point probe.

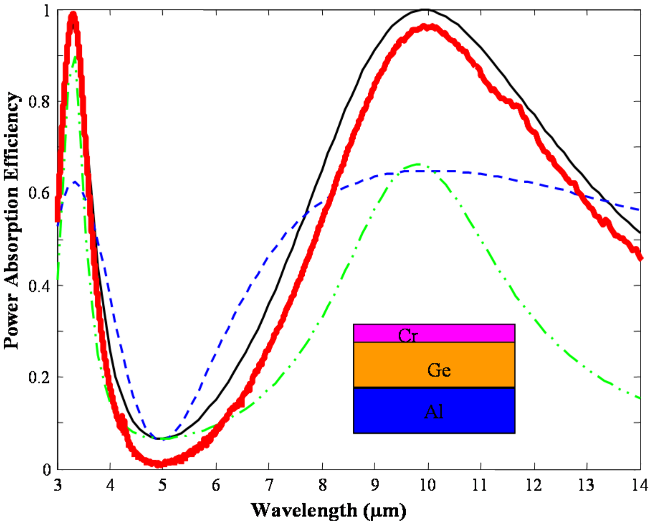

Figure 2.13: A comparison of spectral responses of FTIR-microscope-measured absorption data (red curve) for Ge-layered Salisbury Screen with a Ge thickness of 0.62μm and a Cr thickness of 18 nm and plane wave calculations for Ge-layered Salisbury Screen with three different sheet resistances: dc sheet resistance R_s = 400Ω/□ (black curve), dc sheet resistance R_s = 100Ω/□ (blue-dashed curve), and dc sheet resistance R_s = 2800Ω/□ (green-dashed-dotted-dotted curve).

Also, using Cr as the absorber for the modified DSS (air gap structure) is a good choice. Figure 2.14 shows the measured FTIR microscope absorption data (black solid curve) for the modified DSS with a thickness of Ge d_1 = 0.6μm, air gap thickness d_2 = 4.8μm, and Cr absorber layer (R_s = 400Ω/□); it compares this with the plane wave calculations for the same structure with three different sheet resistances. The fabricated modified DSS device has a sheet resistance R_s = 400Ω/□.; the measured data should thus agree with the plane wave calculation with R_s = 400Ω/□ (blue-dashed curve). The absorption resonance for the fabricated modified DSS device matches the plane wave calculation. It produces, however, less absorption than the plane wave calculation with R_s

= 400Ω/□. The sheet resistance of the resistive absorber layer is a key factor in controlling the power absorption of the modified DSS device. The plane wave calculation model for low sheet resistance R_s = 100Ω/□ (red dotted curve) has almost the same power absorption efficiency (0.68) as the measured data. At wavelengths 10µm and 6µm, however, the bandwidths of, respectively, the main and second absorption curves are broader than the measured data. Also, the plane wave calculation model for high sheet resistance R_s = 3000Ω/□ (green dashed-dotted curve) has almost the same power absorption efficiency as the measured data. At wavelength 10µm, however, the bandwidth of the main absorption curve is narrower than the measured data.

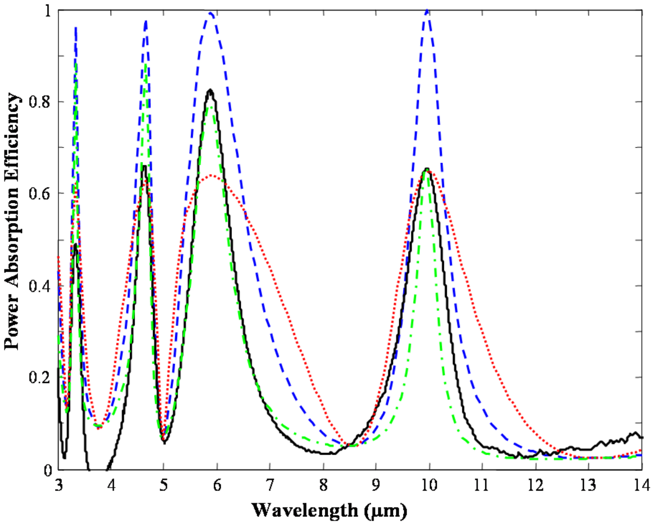

Figure 2.14: Spectral responses of FTIR-microscope-measured absorption data (black solid curve) for modified DSS with thickness of Ge d_1 = 0.7µm, air gap thickness d_2 = 4.9µm, and Cr absorber layer (R_s = 400Ω/□) compared to plane wave calculations for the same structure with three different sheet resistances: dc sheet resistance R_s = 400Ω/□ (blue dashed curve); dc sheet resistance R_s = 100Ω/□ (red dotted curve); and dc sheet resistance R_s = 3000Ω/□ (green dashed-dotted curve).

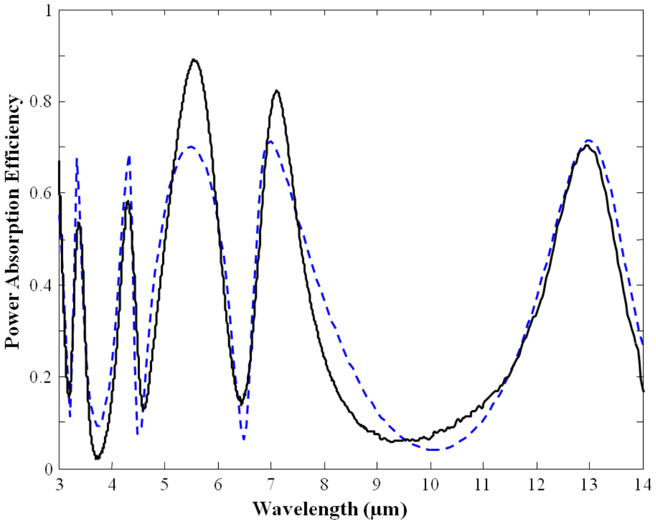

Figure 2.15: Spectral responses of FTIR-microscope-measured absorption data (black solid curve) for modified DSS with thickness of Ge d_1 = 0.7μm, air gap thickness d_2 = 6.6μm, and Cr absorber layer (R_s = 120Ω/□) compared to plane wave calculations for same structure with dc sheet resistance R_s = 120Ω/□ (blue dashed curve).

The fabricated modified DSS devices with two different sheet resistances were measured to confirm that the sheet resistance of absorber layer affects the power absorption of devices. For example, in the case of a sheet resistance lower than Rs = 400Ω/□, Figure 2.15 shows that when the sheet resistance of the Cr absorber layer is 120 Ω/□ good agreement exists between the measured data and the plane wave calculation. Power absorption efficiency is not reduced when we lower the sheet resistance to less than Rs = 400Ω/□. When sheet resistance is higher than Rs = 400Ω/□, the main peak of the absorption curve at wavelength 13.5μm (black solid) agrees with plane wave calculation with Rs = 2800Ω/□ (blue-dashed curve). The peaks of the absorption curve at short wavelengths, however, drop compared to the plane wave calculation. Nevertheless, lower sheet resistances are able to sustain the power absorption efficiency of that for sheet resistance R_s = 400Ω/□.

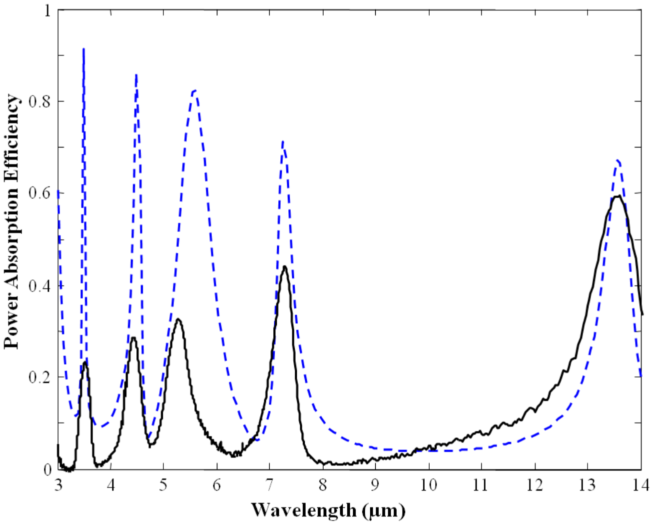

Figure 2.16: Spectral responses FTIR-microscope-measured absorption data (black solid curve) for modified DSS with thickness of Ge d_1 = 0.7μm, air gap thickness d_2 = 6.95μm, and Cr absorber layer (R_s = 2800Ω/□) compared to plane wave calculations for same structure with dc sheet resistance R_s = 2800Ω/□ (blue dashed curve).

It is confirmed that sheet resistance R_s = 400Ω/□ of the Cr absorber layer behaves in the LWIR band the same as dc sheet resistance R_s = 400Ω/□. The measurement of the Ge-layered Salisbury Screen, shown in Fig. 2.13, confirms that sheet resistance R_s = 400Ω/□ of Cr absorber layer behaves in the LWIR band the same as the dc sheet resistance $R_s = 400\Omega/\square$. Therefore, the modified DSS with sheet resistance $R_s = 400\Omega/\square$ of Cr absorber layer is supposed to produce better absorption than the measured data. Since the modified DSS is a free standing MEMS structure, it's possible that, after the sacrificial layer is removed, the Ge dielectric layer (free standing membrane) of the modified DSS may not be completely flat. It is assumed that a difference in air gap thickness exists for the modified DSS. Figure 2.17 shows the FTIR-measured data (black curve) for the modified DSS with Ge thickness $d_1 = 0.7\mu m$, air gap thickness $d_2 = 4.9\mu m$, and Cr absorber layer ($R_s = 400\Omega/\square$); the figure compares it with plane wave calculations. Agreeing well with measured data is the average of the power absorption curve (red curve) for five different air gap thicknesses: 4.7μm, 4.8μm, 4.9μm, 5μm, and 5.1μm. The differences in air gap thickness amount to 4%. If we divide the curves of power absorption by 5, for each air gap thickness as shown in Fig. 2.17, we see that the peak of the absorption curve for each air gap thickness is very resonant and sensitive. That's why the peaks of the absorption curve drop down and its valleys rise up. In the case of sheet resistance $R_s = 120\Omega/\square$, lower than $R_s = 400\Omega/\square$, Figure 2.18 shows excellent agreement between the measured data (black curve) and the plane wave calculated average power absorption of 5 different air gap thicknesses (red curve), those being 6.4μm, 6.5μm, 6.6μm, 6.7μm, and 6.8μm. The power absorption peak for the modified DSS with sheet resistance $R_s = 120\Omega/\square$, shown in Fig. 2.15 (black and blue curve), is broader than that for the plane wave calculated modified DSS with sheet resistance $R_s = 400\Omega/\square$, shown in Fig. 2.14 (blue-dashed curve). The power absorption peak of the former is less resonant and less sensitive than that of the latter. Because of this, the peak of power absorption stays constant.

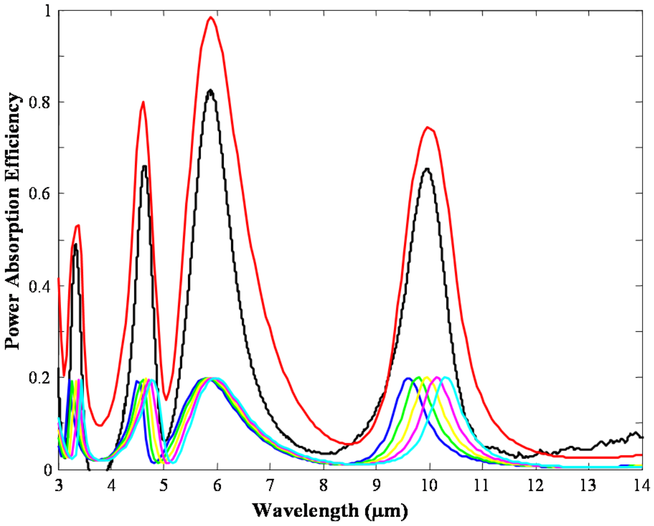

Figure 2.17: Spectral responses of FTIR-microscope-measured absorption data (black curve) for modified DSS with thickness of Ge d_1 = 0.7μm, air gap thickness d_2 = 4.9μm, and Cr absorber layer (R_s = 400Ω/□) compared to plane wave calculated average of power absorption curve (red) for five different air gap thicknesses; power absorption divided by 5 for air gap thickness d_2 = 4.7μm (blue); power absorption divided by 5 for air gap thickness d_2 = 4.8μm (green); power absorption divided by 5 for air gap thickness d_2 = 4.9μm (yellow); power absorption divided by 5 for air gap thickness d_2 = 5μm (magenta); and power absorption divided by 5 for air gap thickness d_2 = 5.1μm (cyan).

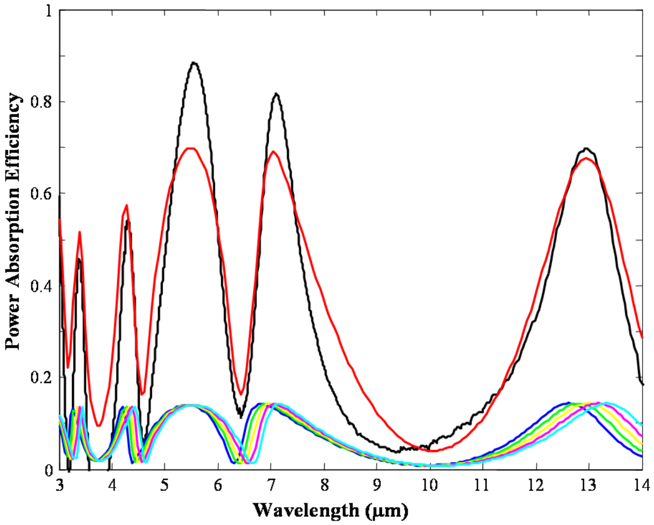

Figure 2.18: Spectral responses of FTIR-microscope-measured absorption data (black curve) for modified DSS with thickness of Ge d_1 = 0.7µm, air gap thickness d_2 =6.6µm, and Cr absorber layer (R_s = 120Ω/□) compared to plane wave calculated average of power absorption curve (red) for five different air gap thicknesses; power absorption divided by 5 for air gap thickness d_2 = 6.4µm (blue); power absorption divided by 5 for air gap thickness d_2 = 6.5µm (green); power absorption divided by 5 for air gap thickness d_2 = 6.6µm (yellow); power absorption divided by 5 for air gap thickness d_2 = 6.7µm (magenta); and power absorption divided by 5 for air gap thickness d_2 = 6.8µm (cyan).

Three different FTIR microscope field positions with 30 µm x 30 µm field sizes on 150 µm x 150 µm size pixel of device are measured to make sure that there is no difference in air gap thickness. Figure 2.19 illustrates that there is a difference in air gap thickness for 150 µm x 150 µm size pixel of device. Each peak of power absorption for each field position is very close to each other.

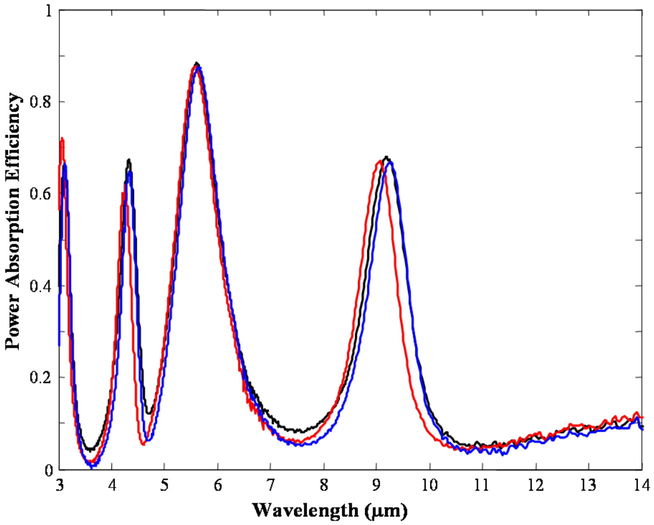

Figure 2.19: Spectral responses of three different FTIR microscope field positions with 30 μm x 30 μm field sizes on 150 μm x 150 μm size pixel of device.

Figure 2.20 shows that the design rules for modified DSS as shown in Fig. 2.5 work well. The thickness of Ge dielectric layer for two different devices is about a quarter-wavelength of the center wavelength, and the thickness of air gap for two different devices is a half-wavelength of the center wavelength.

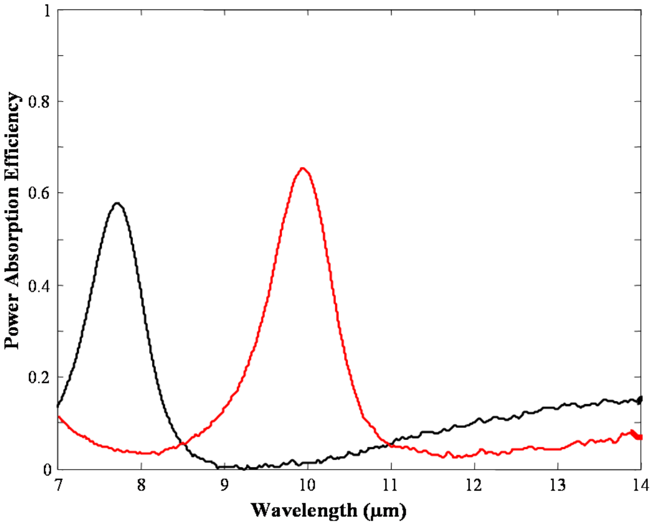

Figure 2.20: Spectral responses of measured data that prove the design rules for the modified DSS, shown in Fig. 2.5, work well; modified DSS (black curve) with thickness of Ge $d_1 = 0.5\mu m \approx (\lambda_c/n)/4$, air gap thickness $d_2 = 3.8\mu m \approx \lambda_c/2$, and Cr absorber layer (R_s = 400Ω/□); modified DSS (red curve) with thickness of Ge $d_1 = 0.6\mu m \approx (\lambda_c/n)/4$, air gap thickness $d_2 = 4.8\mu m \approx \lambda_c/2$, and Cr absorber layer (R_s = 400Ω/□).

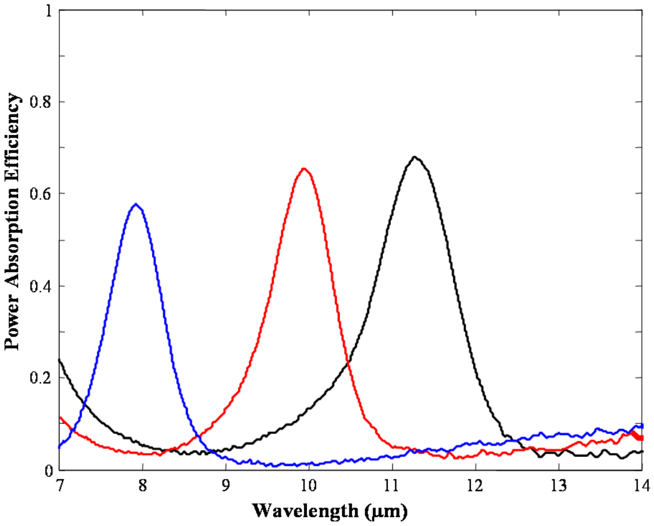

Figure 2.21: Spectral responses of measured data for varying air gap thickness while the sheet resistance R_s = 400Ω/□ of Cr absorber layer and thickness of Ge d_1 = 0.7μm are fixed; the power absorption curve for air gap thickness d_2 = 3.8μm (blue); the power absorption curve for air gap thickness d_2 = 4.8μm (red); the power absorption curve for air gap thickness d_2 = 5.6μm (black).

The modified DSS structure is air-gap–tunable; i.e., by varying only the air gap the center wavelength is shifted (tuned), as shown in Figs. 2.7 and 2.21. For fixed thickness of Ge d_1 = 0.7μm, the center wavelength of the absorption curve for air gap thickness d_2 = 3.8μm (blue) is about wavelength 8μm, the center wavelength of the absorption curve for air gap thickness d_2 = 4.8μm (red) is about wavelength 10μm, and the center wavelength of the absorption curve for air gap thickness d_2 = 5.6μm (black) is about wavelength 11.5μm.

2.5 CONCLUSIONS

The measured spectral responses of fabricated modified DSS agree well with plane wave calculation models. The design rules show that the quarter-wavelength dielectric thickness and the half-wavelength air gap thickness with the proper sheet resistance of absorber layer produce excellent tunable narrowband power absorption. The key factor to producing better power absorption is controlling the flatness of dielectric support layer.

Chapter 3: Cross Patterned Resistive Sheets

I discuss here a cross-shaped patterned resistive sheet as a frequency-selective absorber. It is used in long wave infrared (LWIR) microbolometer focal plane arrays. These cross-patterned resistive sheets are essentially slot antennas formed in a resistive ground plane layer having an optimized sheet resistance. They are placed a quarter-wavelength in front of a mirror. In addition, for realistic metal layers the skin effect produces complex surface impedance that, in the LWIR band, can be quite large. Also, the relaxation time in the LWIR produces complex AC conductivity. Instead of a thin resistive sheet layer as the absorber layer, I consider in this paper metal layers of finite thickness. Finite thickness metal layers, I will show, can still produce excellent absorption in the LWIR.

3.1 METHOD OF MODIFIED EISENHART & KHAN MODEL

To achieve a narrowband spectral response with the simplest possible fabrication process, this paper puts forward a patterned resistive sheet as the frequency-selective absorber. These patterned resistive sheets are a modified form of classical Salisbury Screens. Salisbury Screens utilize a resistive absorber layer placed a quarter-wavelength in front of a mirror. As shown in Fig. 3.1, there are five basic design parameters for these structures: array period a, air gap thickness d, the dimensions of "holes" g and w, and sheet resistance of the resistive sheet R_s. Previously designed planar antenna-coupled microbolometers consisted of both resistive and highly conductive metal strips (acting as antennas) [17].The absorption layer in these structures, by comparison, involves only one resistive layer with patterned holes. We have developed a modified mode-matching technique to model the electromagnetic response of these patterned resistive sheets to achieve the required narrowband IR response [18]. For the more general case, the design space consists of four geometrical parameters (the period, two dimensions for rectangular holes, and the distance to the mirror) and one sheet resistance parameter. The modified mode-matching technique is thus ideally suited for rapid multi-variate optimization. To verify the results of this design optimization, the spectral response has also been calculated using HFSS, an industry-standard, full-wave finite element method EM solver. If R_1=0 in the two circuit models in Figure 4, both circuit models are identical to the original Eisenhart & Khan models [19]. In a patterned resistive sheet structure, the metal grids of the planar multimode detectors are replaced with finite sheet resistance sheets. R_1 represents an additional equivalent resistance due to the resistive sheet. R_1 could be added to the Eisenhart & Khan models in two ways—series or shunt. To determine which, if either, of these models is approximately correct, full wave FEM simulations have been compared to those from the modified analytical Eisenhart & Khan model. Typical results are illustrated in Fig. 3.1. The red curve in Fig. 3.1 is a simulated result from HFSS. The blue curve is the result from the modified analytical Eisenhart & Khan model using circuit model 1. The green curve is from circuit model 2. For design purposes, the modified model 1 appears to be the better fit. This is because main losses are due to current flow in sheet; such losses are related to the inductive component rather than the capacitive part.

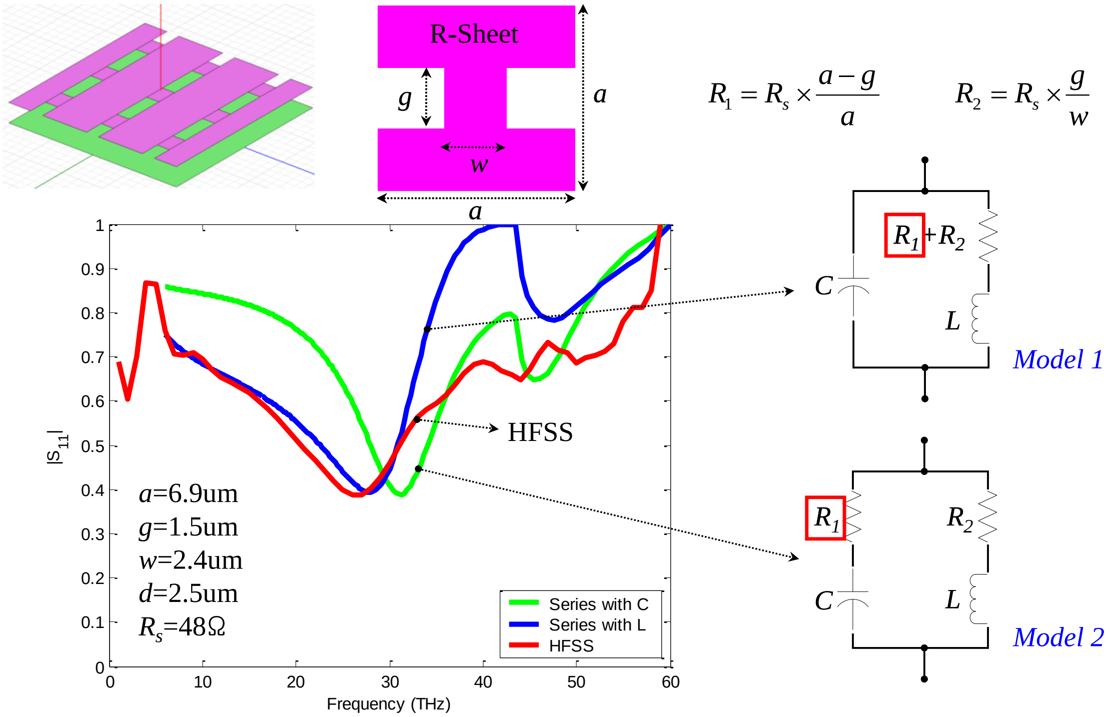

Figure 3.1: Comparison between HFSS full wave calculations and modified analytical Eisenhart & Khan model of a patterned resistive sheet.

The LWIR spectral response of a patterned resistive sheet structure is the result of complex interactions between all design parameters, including the shape of the hole. To find a desired response requires the use of a multi-variate numerical optimization process, such as the Genetic Algorithm (GA). HFSS may be very difficult to use for numerical optimization because of its long calculation time. For such design optimization we use the modified Eisenhart & Khan model for calculation of the patterned resistive sheet spectral response. This model, however, is not as accurate as HFSS. The modified Eisenhart & Khan model actually agrees reasonably well with HFSS based on several comparisons of simulated results from both methods. Figure 3.2 shows the configuration of a GA-optimized patterned resistive sheet structure designed for narrow band absorption at 10µm. The spectral response found from the E & K model (blue) shows good agreement with HFSS (red). The patterned resistive sheet structures can provide much narrower bandwidth for wavelength selectivity than a simple uniform resistive sheet (i.e., simple Salisbury Screen shown by the dotted curve).

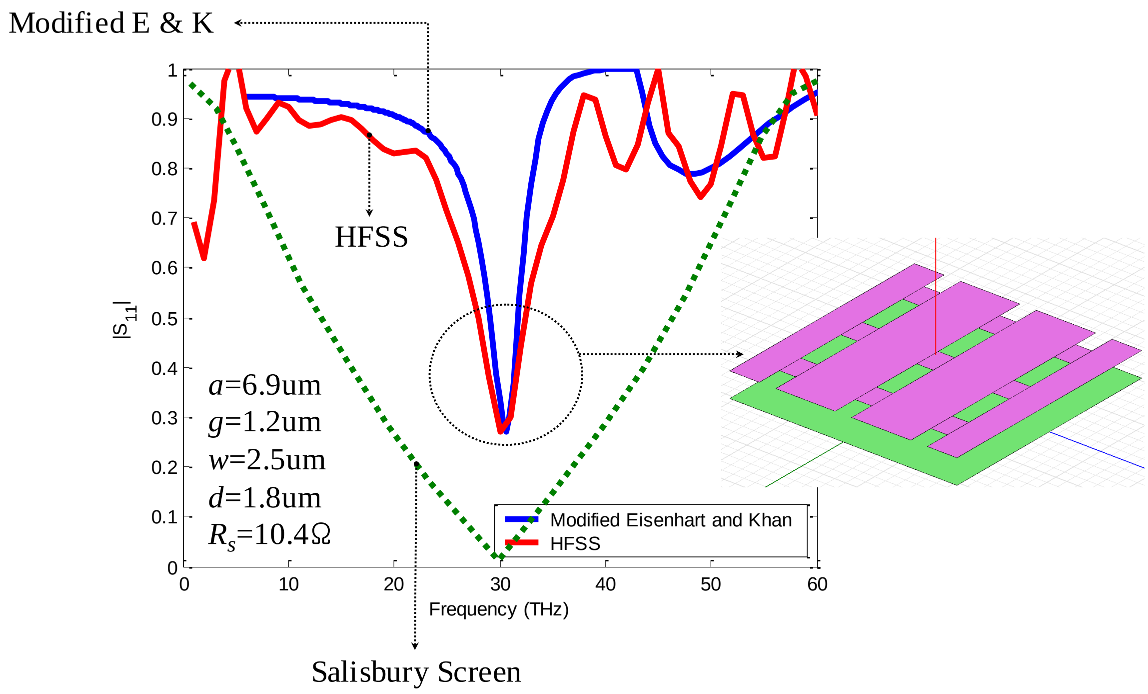

Figure 3.2: GA-optimized narrow band absorption produced by the patterned resistive sheet structure. Good agreement between HFSS (red) and modified Eisenhart and Khan's model (blue) is observed. The patterned resistive sheet structures can provide much narrower bandwidth for wavelength selectivity than simple uniform resistive sheets (Salisbury Screen: dotted curve).

3.2 DESIGN FOR WAVELENGTH SELECTIVE ABSORPTION USING A FREQUENCY SELECTIVE SURFACE

3.2.1 Rectangular Slot FSS Bandpass Filters

While the speed of the modified Eisenhart & Khan model for design optimization surpasses that of HFSS, its accuracy does not. Therefore, I have developed an alternative method to design patterned resistive sheet structures. If we consider only the absorption layer (resistive layer) in free space, and replaced the resistive sheet with a perfectly conducting layer, as illustrated in Fig. 3.3 (a), it looks like a frequency selective surface (FSS) consisting of a perfectly conducting sheet with periodic rectangular patterned slots.

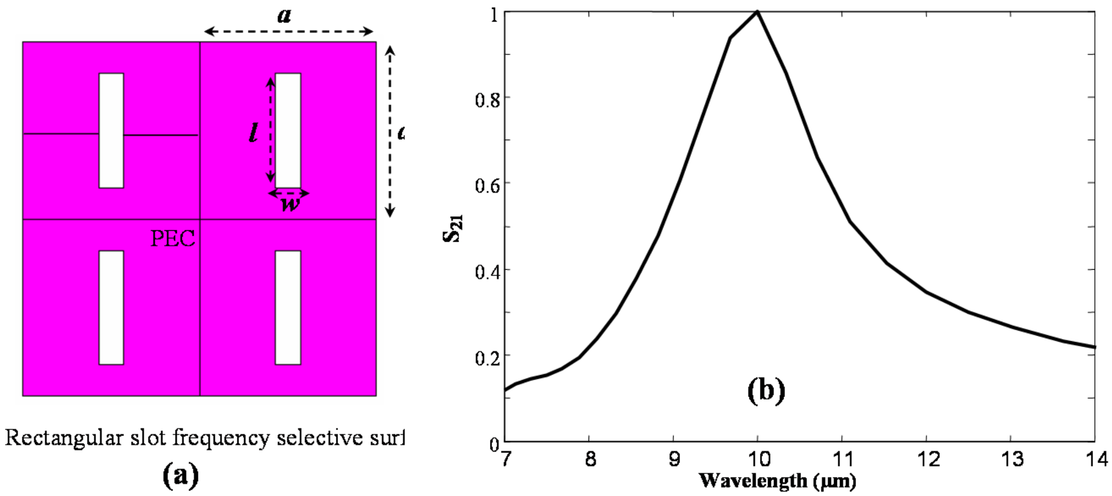

Figure 3.3: (a) Rectangular slot frequency selective surface (FSS) bandpass filter. (b) HFSS calculated spectral response for bandpass filter for w = 0.4μm, l = 4.6μm, and a =6.9μm.

For wavelengths greater than array period a, such a rectangular slot FSS behaves as a bandpass filter [10]. A single rectangular slot produces a transmission resonance at approximately [10, 20]

$$\lambda_{res} = 2.1(l + \frac{w}{2}) \tag*{eq. 1}$$

For example, in Fig. 3.3 if we set w = 0.4µm, l = 4.6µm, and a = 6.9µm, then the resonance wavelength for a single slot is 10µm. In an array there is an interaction between the slots; this is evidenced by the transmission resonance shift shown in Fig. 3.3 (b).

3.2.2 Dependence of Sheet Resistance of Patterned Resistive Absorber Layer

The goal here is to use the FSS bandpass filter design as a narrow band wavelength selectivity absorber in a microbolometer structure. We do so by placing the FSS approximately one quarter wavelength in front of a mirror. Figure 3.4 illustrates the behavior of a FSS designed to produce resonance at a wavelength of 10 µm. In general, the length of the slot primarily determines the resonance wavelength, while the resonant absorption wavelength is weakly dependent on the gap between the patterned resistive absorber and the mirror. Nonetheless, setting this gap to be approximately a quarter-wavelength at the peak of the absorption curve (as in a normal Salisbury screen) typically produces the strongest absorption.

The dependence of the spectral response on sheet resistance R_s is more complex. We find in Fig. 3.4 the HFSS^{TM} finite-element-method electromagnetic calculated spectral response for the patterned resistive sheet structure for array period a = 6.9µm, width of rectangular slot w = 0.4µm, and length of rectangular slot l = 4.6µm. Here R_s is varied from a perfect electric conductor (PEC) to 3Ω/□ while the gap distance d is fixed at 2.5µm. When R_s is zero (i.e., it is a PEC), it should not absorb any power; the HFSS^{TM} calculated reflection coefficient curve (red) is, for this case, essentially one, and the corresponding absorption is essentially zero.

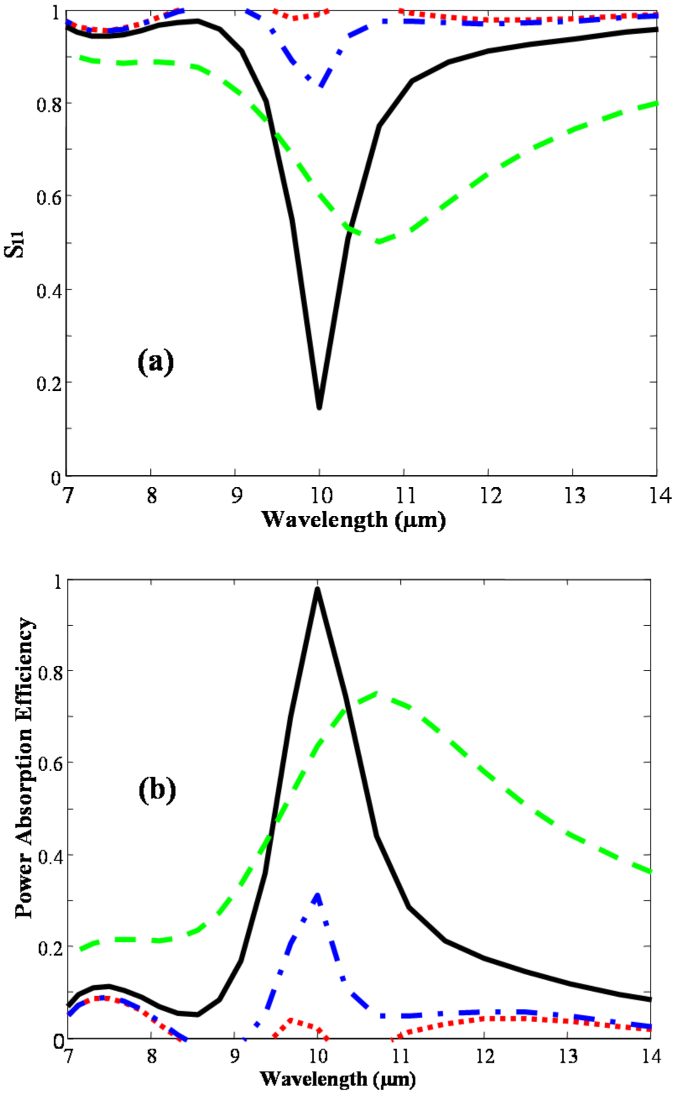

Figure 3.4: Spectral responses as a function of R_s for a patterned resistive sheet structure for width of rectangular slot w = 0.4μm, length of rectangular slot l = 4.6μm, array period a = 6.9μm, and thickness of gap d = 2.5μm: the sheet resistances of the patterned resistive sheet layer is: 0Ω/□ (red dotted curve); 0.1Ω/□ (blue dash-dotted); 1Ω/□ (black solid); and 3Ω/□ (green dashed); (a) magnitude of reflection coefficient $|S_{11}|$; (b) power absorption calculated from $1\text{-}S_{11}^2$.

Figure 3.4 shows that for sheet resistance $R_s = 1\Omega/\square$ (black) absorption of almost all incident power at the center wavelength of 10μm is achieved. Note that varying the sheet resistance R_s has little effect on the center wavelength of the resonant power absorption. When low sheet resistance ($R_s = 0.1\Omega/\square$) is selected, however, there is very weak absorption; with high sheet resistance ($R_s = 3\Omega/\square$), the absorption bandwidth increases.

3.2.3 Cross Patterned Resistive Sheet

The rectangular patterned resistive sheet structure discussed above shows spectral selectivity for only one polarization. Figure 3.5 (b) shows the HFSS^{TM} calculated TE polarization, where the E-field is perpendicular to the length dimension of the rectangular hole in Fig. 3.5 (a). It also shows the TM (orthogonal) polarization, for a normal incident plane wave. As would be expected, only the TE polarization, when the H field is aligned along the long dimension of the slot, is strongly absorbed for this structure. To achieve a narrowband spectral response with a less polarized independent response, I discuss here the use of a cross patterned resistive sheet as a frequency-selective absorber. Figure 3.6 (a) shows the configuration of the cross patterned resistive sheet structure. The dimensions of cross slot are from the rectangular patterned resistive sheet design. The HFSS calculated spectral response in Fig. 3.6 (b) shows the cross patterned resistive sheet with both TE and TM polarization (black solid curve) absorbs almost unit power at wavelength 10μm. The absorption curve of the cross patterned resistive sheet with 45-degree polarization (red dotted curve) shifts slightly to a shorter wavelength (around wavelength 9.8μm). Nevertheless, the cross-patterned sheet structure with 45-degree polarization absorbs nearly as much power as the cross-patterned resistive sheet with both TE and TM polarization.

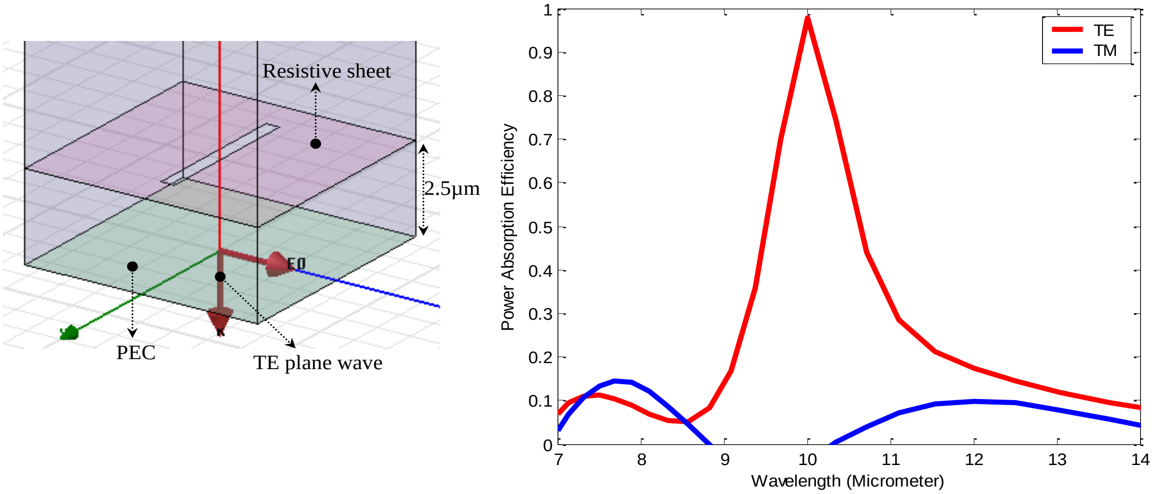

Figure 3.5: (a) Configuration of rectangular patterned resistive sheet structure to see dependency of spectral response on polarization. (b) Spectral responses as function of polarization for $w = 0.4\mu m$, $l = 4.6\mu m$, $a = 6.9\mu m$, and $R_s = 1\Omega$.

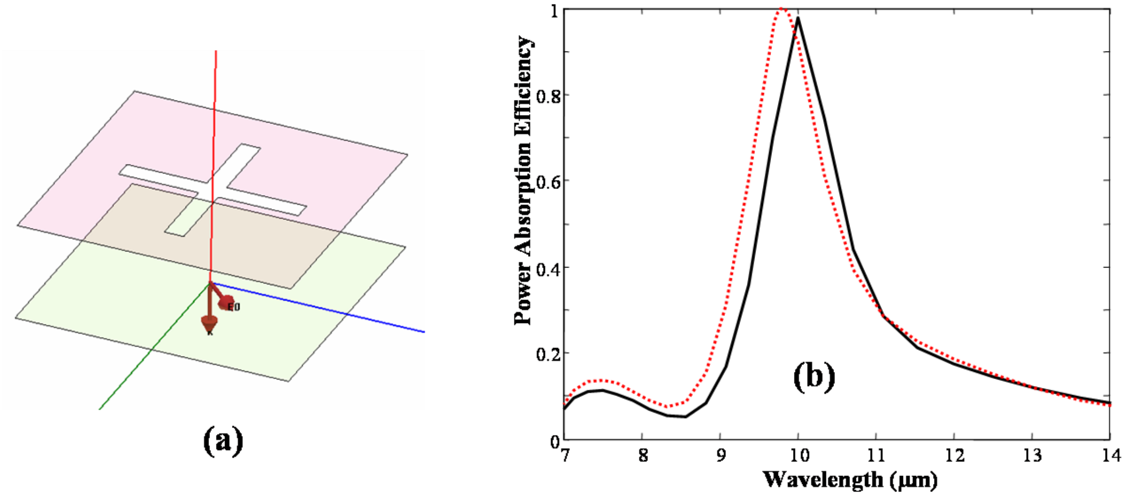

Figure 3.6: (a) Configuration of cross patterned resistive sheet structure. (b) Spectral response of cross patterned resistive sheet for slot dimensions from a rectangular patterned resistive sheet; the absorption spectral response of either the TM or TE polarization (black solid curve); the absorption spectral response of the 45 degree polarization (red dotted).

3.2.4 Dependence of the Width of Slot

As expected based on the FSS literature [9-11, 20], the width of slot w affects the bandwidth of curve. Figure 3.7 shows the HFSS^{TM}-calculated spectral responses for varying widths of the slot. For each width we selected a sheet resistance that would produce maximum peak absorption. For fixed slot length (l = 4.6μm), the resonance wavelength shows minimal change as the width is varied. As the width of the slot increases, the bandwidth of the curve increases. To maintain high absorption efficiency, a wider slot width also requires a larger sheet resistance to produce strong absorption.

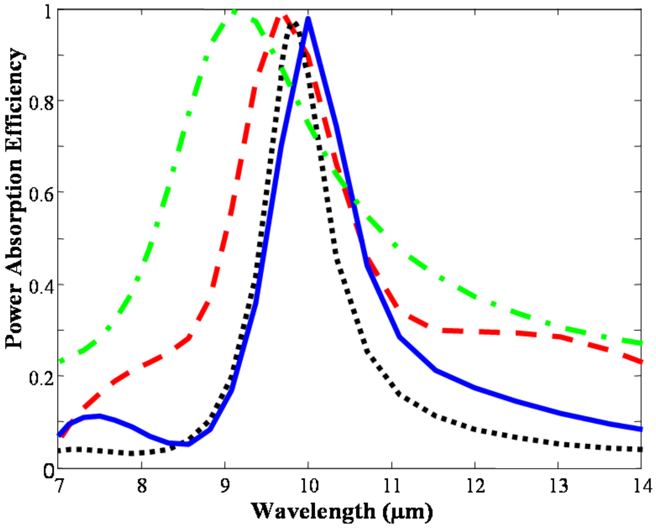

Figure 3.7: Spectral responses of varying width of slots with optimized sheet resistance, but fixed length of slot *l* = 4.6µm, array period *a* = 6.9µm and thickness of gap *d* = 2.5µm: widths with optimized sheet resistance are: 0.2µm with 0.5Ω/□ (black dotted curve); 0.4µm with 1Ω/□ (blue solid); 0.8µm with 3Ω/□ (red dashed); and 1.6µm with 9Ω/□ (green dash-dotted).

3.2.5 Dependence of the Air Gap distance

In Chapter 2, we saw that a modified dielectric-coated Salisbury Screen could, if we changed the air gap distance, achieve multi-spectral response. Hence, one way to obtain multi-spectral response from a patterned resistive sheet structure might be by changing air gap distance d. Fig. 3.8 shows the HFSS^{TM}-calculated spectral responses for the patterned resistive sheet structure for array period a = 6.9µm, width of cross slot w = 0.4µm, length of cross slot l = 4.6µm, and sheet resistance R_s = 1Ω/□. Air gap distance d is varied from 0.5µm to 3.5µm. Despite being varied, for each distance the peak of absorption curve changes little. Such a result is due to the cross slot length being the primary determining factor in setting the resonance wavelength. We would expect this from the FSS bandpass filter view of how this structure functions.

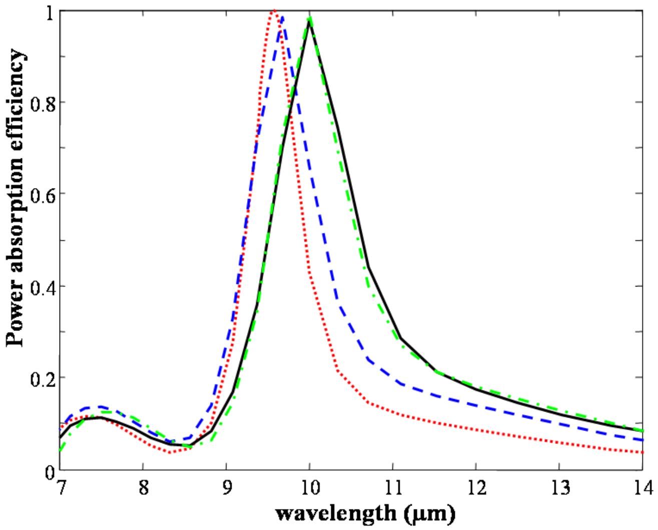

Figure 3.8: Spectral responses as a function of *d* for a patterned resistive sheet structure for width of cross slot *w* = 0.4µm, length of cross slot *l* = 4.6µm, array period *a* = 6.9µm, and sheet resistance R_s = 1 Ω/□: the air gap distance *d* of the patterned resistive sheet layer is: 0.5µm (red dotted curve), 1.5µm (blue dashed), 2.5µm (black solid), and 3.5µm (green dotted-dashed).

3.2.6 Dependence of the Array Period

When the wavelength is greater than the array period, rectangular or cross slot behaviors a bandpass filter. As discussed above I have focused, since LWIR band starts from a wavelength 7µm, on a patterned resistive structure with a fixed array period a = 6.9µm. When the width of cross slot w = 0.4µm and the length of cross slot l = 4.6µm in a cross slot FSS bandpass filter are set, the transmission resonance wavelength is around 10µm, from Equation 1. Figure 3.9 shows the HFSS^{TM} calculated spectral transmission responses of a cross slot FSS bandpass filter with an array period a varying from 5µm to 8µm while the width of cross slot w = 0.4µm and the length of cross slot l = 4.6µm are fixed. The peak of the transmission curve is only weakly dependent on the array period, but as the array period a becomes smaller, the bandwidth of the transmission curve increases. For an array period a = 8μm (green dotted-dashed curve), there is a secondary peak at shorter wavelength; this is most likely due to grating effects at shorter wavelengths when the array period is larger than the wavelength.

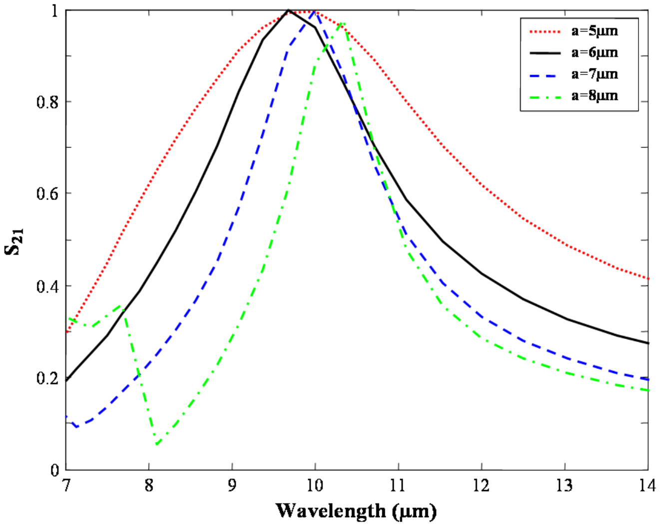

Figure 3.9: Spectral transmission responses (magnitude of S_{21}) as a function of *a* for cross slot FSS bandpass filter for width of cross slot *w* = 0.4μm and length of cross slot *l* = 4.6μm: the array period *a* of the FSS filter is: 5μm (red dotted curve); 6μm (blue dashed); 7μm (black solid); and 8μm (green dotted-dashed). The sheet is assumed to be a PEC.

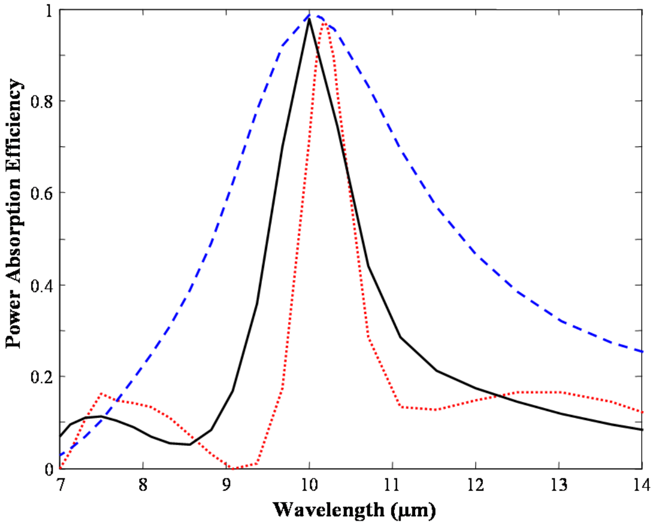

Figure 3.10: Spectral absorption responses of patterned resistive sheet with varying array period with optimized sheet resistance, but fixed length of slot *l* = 4.6μm, width of slot *w* = 0.4μm and thickness of gap *d* = 2.5μm: array period with optimized sheet resistance are: 5μm with 2.5Ω/□ (blue dashed curve); 6.9μm with 1Ω/□ (black solid); and 8μm with 0.5Ω/□ (red dashed).

Figure 3.10 shows the HFSS^{TM} calculated spectral absorption responses of patterned resistive sheets with mirrors placed a fixed distance behind them for varying array periods; for each array period a sheet resistance was selected to produce maximum peak absorption. For fixed slot length and slot width, the resonance wavelength shows, as the array period is varied, minimal change. As the array period decreases, the bandwidth of the curve increases. To maintain high absorption efficiency, a smaller array period also requires a larger sheet resistance to produce strong absorption.

3.3 THREE COLOR DESIGN

For conventional microbolometers it is difficult to produce a multi-spectral focal plane array (one in which different pixels have different wavelength selectivity) due to the broad band spectral response of a conventional Salisbury screen. The only way to produce wavelength selectivity in a simple Salisbury screen microbolometer is to change the gap between the resistive absorber layer and mirror layer. Therefore, to construct a multi-spectral array would require either a different sacrificial layer thickness for the different wavelength pixels in the array or a mechanical actuator for changing gap distance. Meeting such requirements could result in higher costs and a more complex fabrication process. For the resistive sheet cross patterns, however, the center wavelength is set primarily by the dimensions of the cross pattern, not the gap between the absorber and the mirror. To demonstrate the possibility of a simple three color focal plane array, I have applied the constraint that each pixel for each different wavelength uses the same gap thickness d and the same absorber layer sheet resistance R_s. The center wavelength of each pixel is set by selecting the appropriate dimensions of the cross slot. For example, we selected here center wavelengths of 8, 10, and 12µm. Figure 3.11 shows the HFSS^{TM} calculated spectral responses for a three color focal plane design. The three different wavelength selective pixels have a common gap thickness d of 2.5µm, sheet resistance $R_s = 1\Omega/\square$ of absorbing sheet layer, array period a = 6.9µm, and width of slot w of 0.4µm. The only difference between the three pixel designs is the length of cross slot l, which determines the peak absorption wavelength. The pixel for wavelength 8µm (Fig. 3.11, red dotted curve) uses a 3.4µm long slot, the pixel for wavelength 10µm (Fig. 3.11, blue dashed curve) has a 4.6µm long slot, and the pixel for wavelength 12µm (Fig. 3.11, black solid curve) has a 5.8µm long slot. Power absorption efficiencies are almost 100% at each center wavelength, with a sufficiently narrow bandwidth for a LWIR focal plane array with three non-overlapping colors.

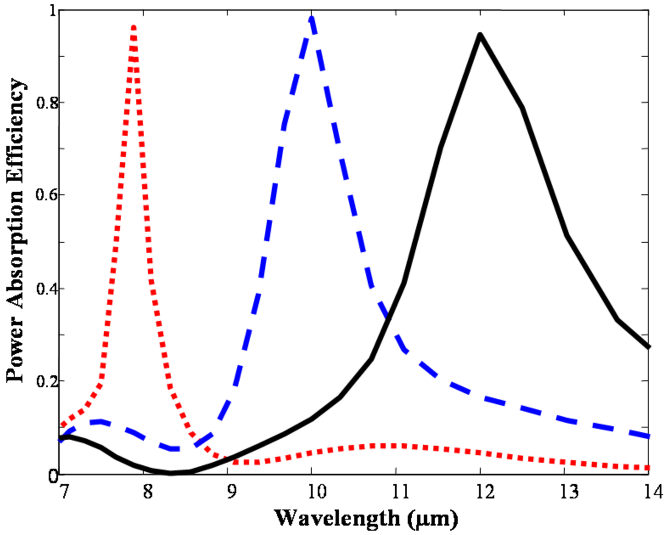

Figure 3.11: Spectral responses for a three-color focal plane design. Each pixel for the different wavelengths has identical design parameters except the length of cross slot *l*, which selects wavelength selectivity: lengths of cross slot are 3.4μm (red dotted curve), 4.6μm (blue dashed), and 5.8μm (black solid).

3.4 FINITE THICKNESS METAL AS AN ABSORBER LAYER

3.4.1 DC Conductivity for metal absorber

Design studies have shown that for efficient IR absorption the patterned absorber layer requires a lossy sheet with a sheet resistance close to 1Ω/□. For realistic metal layers, however, the skin effect produces a complex surface impedance that can be quite large in the LWIR band. Table 3.1 shows electrical dc conductivity, skin depth at wavelength 10μm, and complex surface impedance for metals such as copper, aluminum, and chromium. The thickness of copper metal is around 172Å to get a resistive sheet with dc sheet resistance R_s = 1Ω/□. Also, the thickness of aluminum is around 149Å for dc sheet resistance R_s = 1Ω/□. The thickness of all metals for dc sheet resistance R_s = 1Ω/□ are larger than the skin depth at wavelength 10μm. Therefore, it is not actually possible to make, as the absorber layer in the LWIR band, a “thin” resistive sheet with the surface resistance close to 1Ω/□. To more realistically model a real metal layer, I use a one skin-depth thickness of each metal as the absorber layer. This is simulated using HFSS^{TM} with the option to solve inside of the metal film, which creates mesh points inside the metal film. If the option for solving inside of a metal film in HFSS^{TM} is not used, HFSS^{TM} applies an electrical conductivity to one surface of the metal, where the surface impedance is purely real [21]. Figure 3.12 shows the HFSS^{TM} calculated spectral responses for one-skin-depth thicknesses of each metal. A one-skin-depth thickness (333Å) of chromium as the absorber layer absorbs less power and produces a broader bandwidth because the surface impedance for chromium is larger than the desired sheet resistance R_s = 1Ω/□. Since surface impedances for both copper and aluminum are close to a sheet resistance R_s = 1Ω/□, they still produce excellent narrow bandwidth absorption in LWIR.

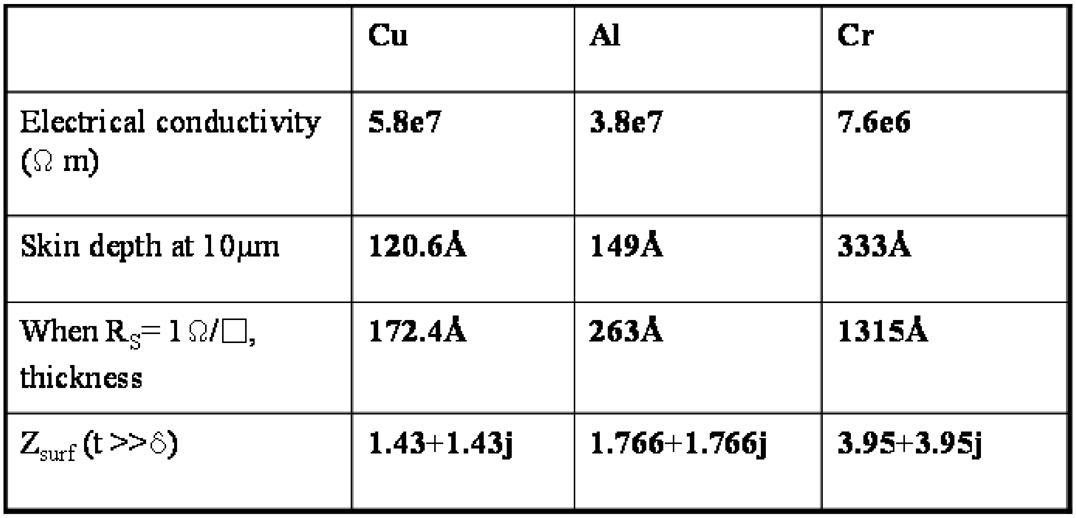

	Cu	**Al**	**Cr**
Electrical conductivity (Ω m)	**5.8e7**	**3.8e7**	**7.6e6**
Skin depth at 10μm	**120.6Å**	**149Å**	**333Å**
When R_S= 1 Ω/□, thickness	**172.4Å**	**263Å**	**1315Å**
Z_{surf} (t >>δ)	**1.43+1.43j**	**1.766+1.766j**	**3.95+3.95j**

Table 3.1: The electrical dc conductivity, skin depth at wavelength 10μm, and complex surface impedance for copper (Cu), aluminum (Al), and chromium (Cr).

The use of a one-skin-depth thickness of copper or aluminum is a good choice for a patterned resistive structure. Figure 3.13 shows the HFSS^{TM} calculated spectral responses for varying copper thickness from one skin depth (120Å) to three skin depths (360Å). Generally, they produce good narrow bandwidth absorption. The bandwidth and peak absorption for a three-skin-depth thickness of metal produces a little narrower bandwidth than that of a metal less than one-skin-depth thick.

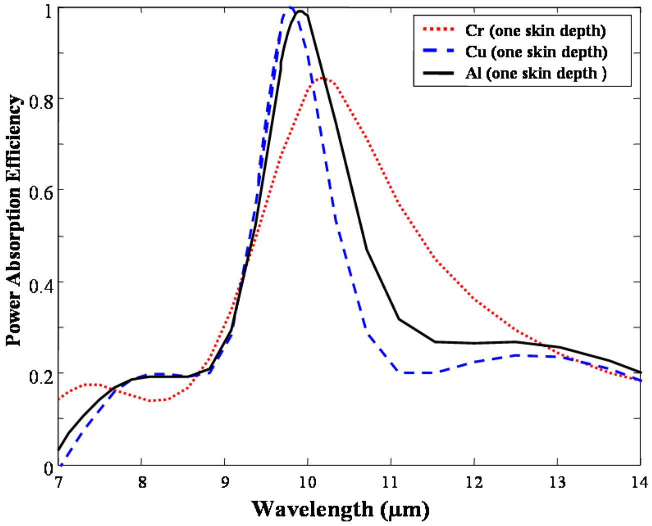

Fig. 3.12: HFSS calculated Spectral responses of one-skin-depth thickness of real metals as absorbers layer for w = 0.4µm, l = 4.6µm, and a = 6.9µm: one-skin depth of aluminum (black solid curve), one-skin depth of copper (blue dashed), and one-skin depth of chromium (red dotted).

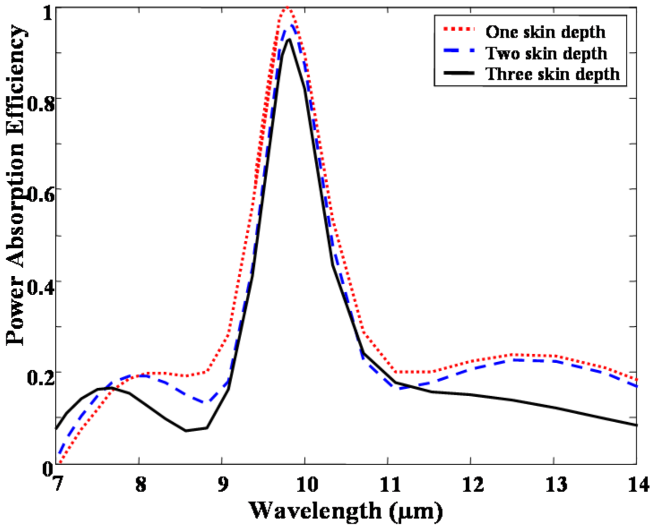

Figure 3.13: HFSS^{TM}-calculated spectral responses of varying thicknesses of copper from a one-skin depth to a three-skin depth, *w* = 0.4μm, *l* = 4.6μm, and *a* = 6.9μm: one-skin depth of copper (red dotted curve), two-skin depth of copper (blue dotted), and three-skin depth of copper (black solid).

As discussed in chapter 3.2.4, to produce a narrower bandwidth requires a narrower cross slot. Simulation results using a thin resistive sheet absorber model require a sheet resistance of less than 1Ω/□ when the width w is less than 0.4μm. It is difficult, using real metals such as copper and aluminum in the LWIR, to get sheet resistance less than R_s = 1Ω/□. The use of real metal as the absorber layer makes narrowing the bandwidth of the absorption curve difficult. Figure 3.14 shows the HFSS^{TM}-calculated spectral responses illustrating this limitation of narrow bandwidth. For fixed width w = 0.1μm, the patterned resistive sheet structure using the metal layer absorbs less than using the sheet resistive layer with sheet resistance R_s = 0.3Ω/□. An even thicker metal layer worsens absorption efficiency.

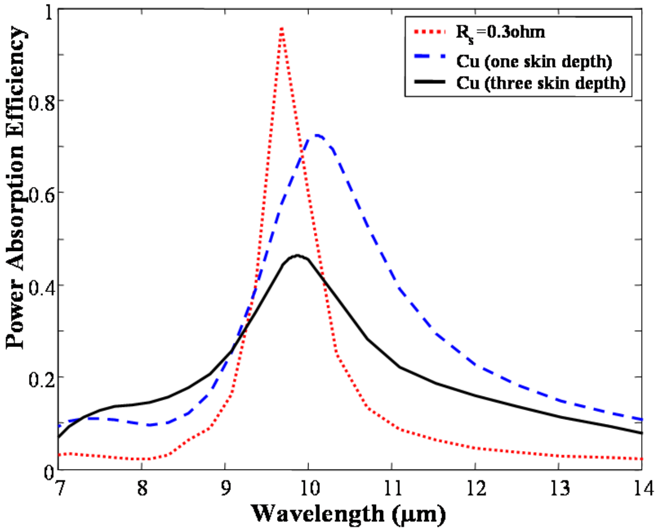

Figure 3.14: Spectral responses showing bandwidth limitation for *w* = 0.1μm, *l* = 4.6μm, *a* = 6.9μm, and *d* = 2.5μm: resistive sheet absorber layer with sheet resistance R_s = 0.3Ω/□ (red dotted curve), one-skin-depth thickness of copper absorber layer (blue dashed), and three-skin-depth thickness of copper absorber layer (black solid).

3.4.2 AC Conductivity for metal absorber

Since the frequency in the LWIR band is on the order of the inverse of the relaxation time for most metals. Because of this, for accurate modeling we should consider the frequency dependent AC conductivity of metals instead of DC conductivity. For example, we use here the AC conductivity of aluminum (Al) described by the Drude model $\sigma = \sigma_0 / (1 + j\omega\tau)$, assuming a DC conductivity $\sigma_0 = 3.8 \times 10^7$ S/m and relaxation time $\tau = 8.0 \times 10^{-15}$ s [15]. Figure 3.15 presents the HFSS^{TM} calculated spectral response of a lossy thin sheet absorber with a sheet resistance of 1Ω/□ (black solid curve) located 2.5 μm in front of a mirror. It compares this to the calculated spectral response of a finite thickness (60 nm) aluminum absorber layer (red dashed curve) located 2.5 μm in front of an aluminum mirror layer (0.2µm thick). The calculations using HFSS^{TM} were performed with the option to solve inside of the aluminum absorber layer, which creates mesh points inside of the metal film. Note that if the option for solving inside of a metal film in HFSS^{TM} is not used, HFSS^{TM} applies an electrical field to the surface of the metal. This implies that the metal film is modeled using the surface impedance of an infinitely thick metal film [21]. The power absorption for the finite thickness Al metal layer used as the absorber is as good as that found for a thin resistive sheet absorber layer. The bandwidth of absorption, however, for the metal absorber is somewhat broadened due to the dispersion induced by the finite relaxation time in the Drude conductivity model for the aluminum.

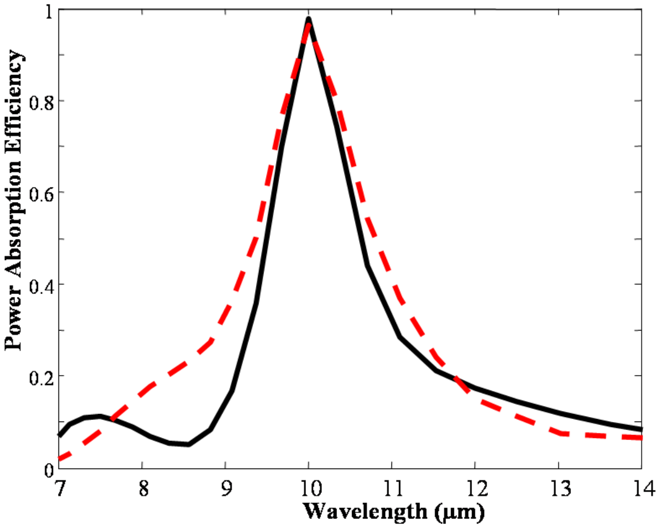

Figure 3.15: Spectral response comparison between a thin lossy sheet absorber with sheet resistance 1Ω/□ (black solid curve) and a finite thickness (60 nm) aluminum absorber layer (red dashed curve): width of cross slot w = 0.4µm, length of cross slot l = 4.6µm, array period a = 6.9µm, and thickness of gap d = 2.5µm.

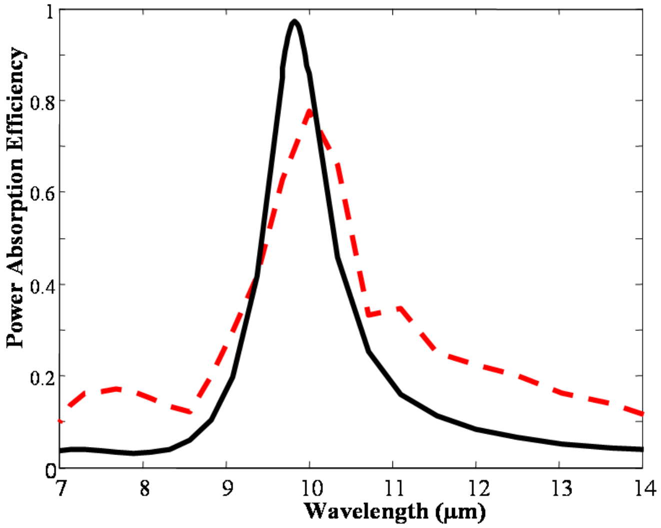

Figure 3.16: Spectral responses showing bandwidth limitation for *w* = 0.2µm, *l* = 4.6µm, *a* = 6.9µm, and *d* = 2.5µm: resistive sheet absorber layer with sheet resistance R_s = 0.5Ω/□ (black solid curve) and finite thickness (60 nm) aluminum absorber layer (red dashed).

As noted above, producing narrower bandwidth requires narrowing the cross slot. Simulation results using a thin resistive sheet absorber model require a sheet resistance of less than 1Ω/□ when width w is less than 0.4µm. Also noted above, however, is the difficulty, when using real metals, to achieve a sheet resistance in the LWIR of less than 1Ω/□. Using a finite thickness metal as the absorber layer makes it difficult to narrow the bandwidth of the absorption curve for such narrow slots. Figure 3.16 shows the HFSS^{TM} calculated spectral responses. It illustrates that when using an AC conductivity model this limitation in bandwidth is similar to what was encountered, in Chapter 3.4.1, when using a DC conductivity model. For fixed slot width w = 0.2µm, the cross patterned resistive sheet structure using a finite thickness (60 nm) of aluminum metal layer (red dashed curve) absorbs less, and produces a somewhat wider bandwidth, than a thin resistive sheet layer with sheet resistance R_s = 0.5Ω/□ (black solid curve).

3.5 DIELECTRIC SUPPORT LAYER

From the perspective of fabrication a patterned resistive sheet structure needs to have a dielectric support layer of certain thickness. Most conventional microbolometers use as a dielectric support layer Si_3N_4. In the LWIR band, $Si_3N_4$is quite dispersive and absorbing [22]. Figure 3.17 (a) shows two different possible structures.

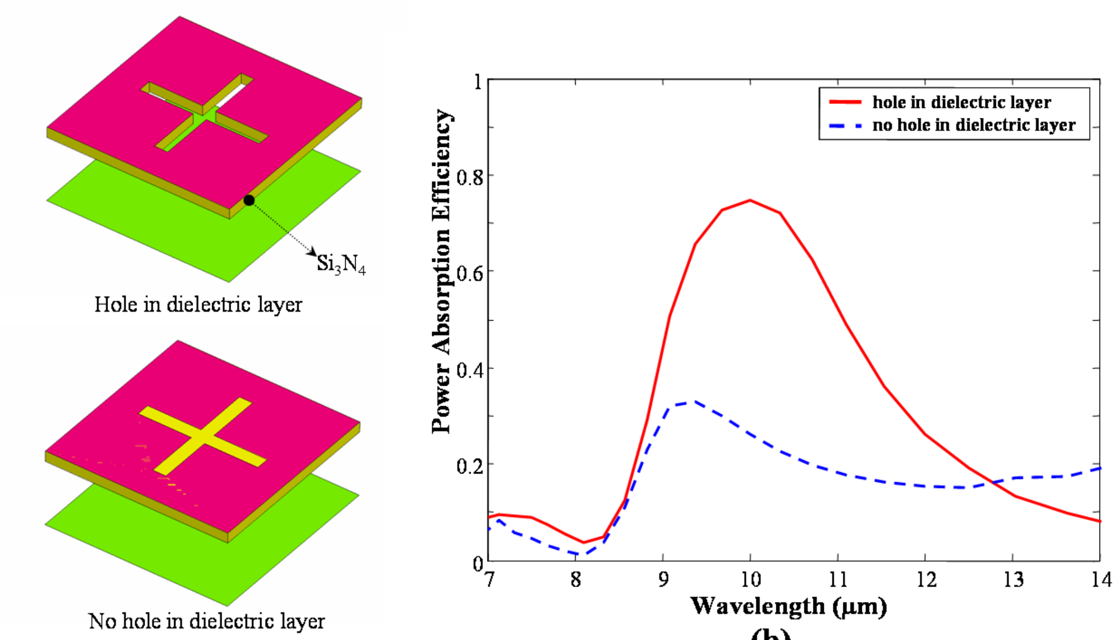

(a) **(b)**

Figure 3.17: (a) configurations of holes in dielectric (Si_3N_4) layer and no hole in dielectric (Si_3N_4) layer. (b) Spectral responses of two structures for w = 0.4µm, l =4.2µm, a = 6.9µm, R_s = 1Ω/□, air gap d = 2.5µm, and, thickness of dielectric t = 0.3µm.

One is a structure that uses a cross patterned hole through both the resistive absorber layer and a support layer of finite thickness (0.3µm). The other is the same cross-patterned hole in the resistive absorber layer but without any of the underlying dielectric layer removed. Figure 3.17 (b) shows HFSS calculated spectral responses of both structures. With no hole through the dielectric, power absorption is strongly affected, due to the interference effects in the dielectric and air gap. For a structure with no hole in the support layer, the center of resonant wavelength shifts and drops. Consider, however, a structure with a cross-shaped hole through both the resistive sheet and the support layer. Here the center wavelength of the resonant absorption stays at about the same wavelength as that produced by a patterned resistive sheet structure without any support layer at all. Even with the holes through the dielectric, since Si_3N_4 is strongly dispersive in the 8μm to 14μm band, the power absorption of a patterned resistive sheet with Si_3N_4 is not as good as that achieved using a non-dispersive, low loss support layer. In the long wave infrared (LWIR), Ge and a-Si:H are examples of such non-dispersive materials [15]. Figure 3.18 (a) shows a cross patterned resistive sheet structure that uses a cross patterned hole through both the aluminum (60nm) absorber layer and through a finite thickness (0.3μm) Ge support layer, mechanically strong enough to be used as a support layer as mentioned in chapter 2. Figure 3.18 (b) shows calculated spectral responses of a structure with the cross-shaped hole through both the metal absorber layer and the dielectric support layer. These are in comparison to a structure with only the cross-patterned metal absorber layer with no dielectric support layer. Note that with no hole through the dielectric support layer a strong dielectric loading effect is evident. In addition, interference effects in the dielectric and gap cause the center of the resonant wavelength to shift to much longer wavelengths (in this case, out of the LWIR band). With a hole through the dielectric support layer, on the other hand, produces a structure with much less effect on the spectral response. Structures with holes through both absorber layer and dielectric support layer produce excellent power absorption when they use aluminum absorbers of the same thickness (60nm) and cross slots of the same size. The centers of the resonant wavelengths, however, shift to wavelengths somewhat longer than those of structures without dielectric support. To return the resonant wavelength back to wavelength 10µm, we must change the cross slot from length l = 4.6µm to l = 3.8µm. Also, decreasing the array period from a = 6.9µm to a = 5.8µm helps remove a secondary peak at shorter wavelengths. This is most likely due to the effective array period being more than 6.9µm due to the dielectric support layer, which at shorter wavelengths leads to grating effects.

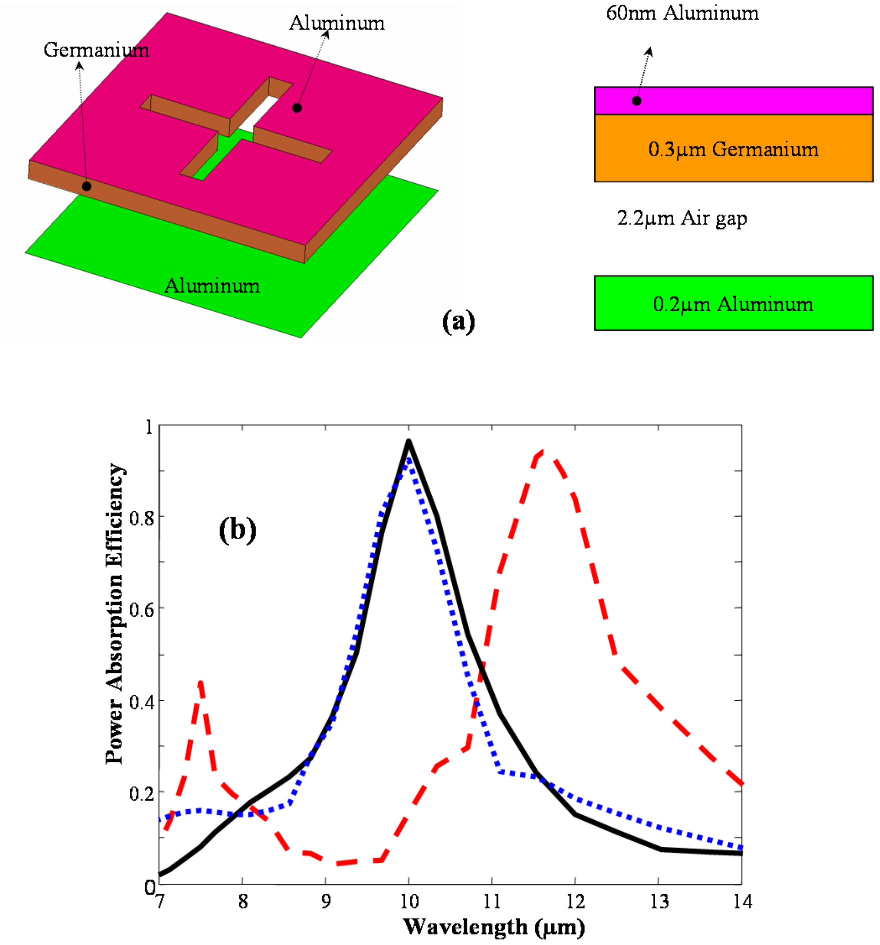

Figure 3.18: (a) Schematic of single unit cell of a cross patterned resistive sheet structure with germanium support layer. (b) Spectral responses with and without dielectric support layer: black solid curve: patterned resistive sheet structure without dielectric support layer, array period a = 6.9μm, length of cross slot l = 4.6μm, width of cross slot w = 0.4μm, thickness of gap d = 2.5μm, and finite thickness (60 nm) aluminum absorber; red dashed curve: patterned resistive sheet structure with hole through both metal absorber layer and dielectric support layer, array period a = 6.9μm, length of cross slot l = 4.6μm, width of cross slot w = 0.4μm, thickness of gap d = 2.2μm, finite thickness (60 nm) aluminum absorber, and finite thickness (0.3μm) germanium support layer; blue dotted curve: patterned resistive sheet structure with hole through both metal absorber layer and dielectric support layer array period, a = 5.8μm, length of cross slot l = 3.8μm, width of cross slot w = 0.4μm, thickness of gap d = 2.2μm, finite thickness (60 nm) aluminum absorber, and finite thickness (0.3μm) germanium support layer.

3.6 CONCLUSIONS

The design of the cross patterned resistive sheets has been investigated for use in wavelength selective long wave infrared (LWIR) focal planes arrays. Cross patterned resistive sheet structure is less independent of polarization. The absorption curve of the cross patterned resistive sheet with 45-degree polarization shifts slightly to a shorter wavelength. The length of cross slot decides the resonance wavelength, and the width of cross slot affects the bandwidth of absorption curve. As the width of the slot increases, the bandwidth of the curve increases. To maintain high absorption efficiency, a wider slot width also requires a larger sheet resistance to produce strong absorption. Cross patterned resistive sheet structures using finite thickness metal layers as the absorber can have high absorption at the designated wavelength and produce enough spectral selectivity to allow a multi-color system spanning the 7-14 micron band.

Chapter 4: Square and Circular Patterned Resistive Sheets for narrow band absorption

An array of square holes in a resistive sheet can act as a frequency selective absorber for use in long wave infrared (LWIR) microbolometer focal plane arrays. This frequency selective surface is placed a quarter-wavelength in front of a mirror. Simulations indicate that metal layers of finite thickness can be used as the absorber layer and produce excellent absorption in the long wave infrared band.

4.1 FREQUENCY SELECTIVE SURFACE BAND PASS FILTER DESIGN APPROACH

In the 1960s, periodic square slots in metal layers (Fig. 4.1) were called metallic mesh inductive grids; they were used as filters [7, 8]. For wavelengths greater than the array period a, a periodic square hole pattern in a perfectly conducting layer could act as a frequency selective bandpass filter with a peak transmission at a wavelength near the array period [8]. Figure 4.1 shows the HFSS^{TM} calculated reflection coefficient curve (red dotted) and transmission coefficient curve (black solid) for array period a = 9.3μm, and square hole side length l = 3.72μm. The resonance wavelength for square slot FSS filter occurs near array period at 9.7μm.

As shown in Fig. 4.2, there are four basic design parameters for square-shaped patterned resistive sheet structures: array period a; air gap distance d to the mirror; square hole side length l; and resistive sheet resistance R_s. For a patterned resistive sheet the behavior is similar to the band pass filter, with peak absorption at a similar wavelength to the peak in transmission. In general, maximum absorption occurs when the patterned sheet is placed approximately a quarter-wavelength (at the peak of the absorption curve) in front of a mirror.

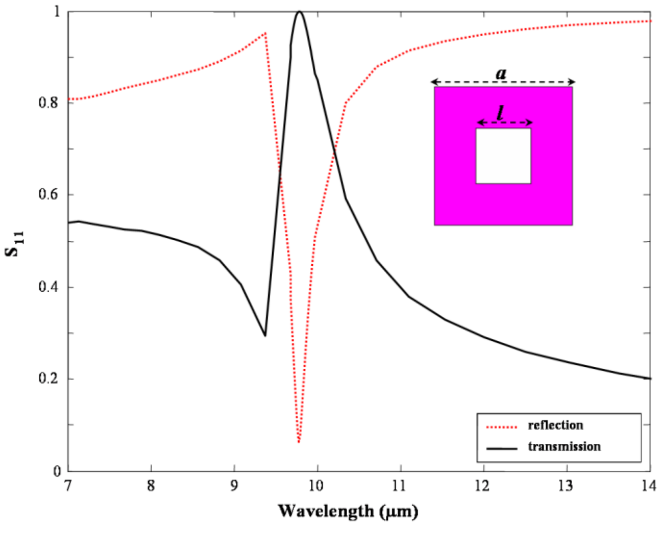

Figure 4.1: Square slot frequency selective surface (FSS) bandpass filter and HFSS calculated spectral response for bandpass filter for *l* = 3.72µm, and *a* =9.3µm.

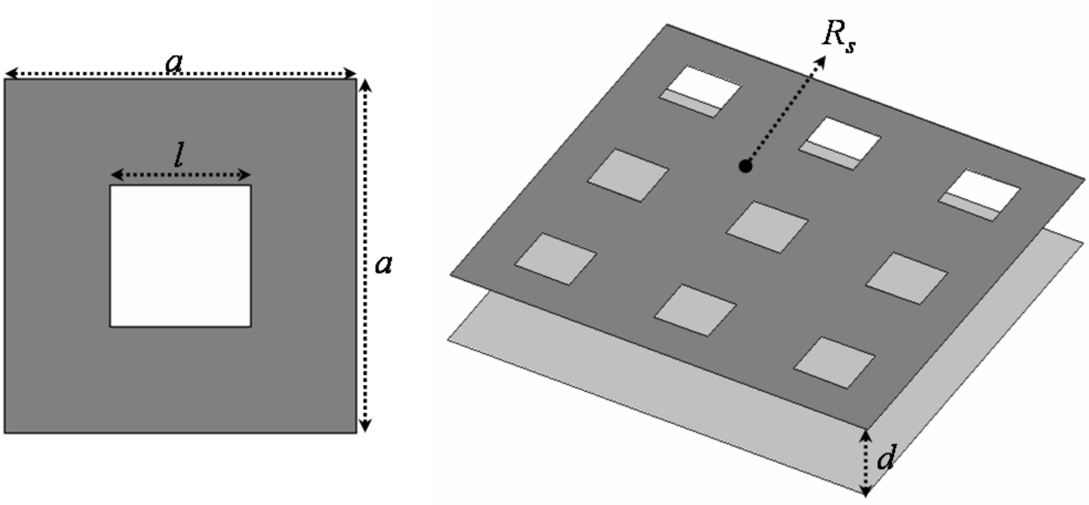

Figure 4.2: Schematic of single unit cell of a square hole patterned absorber layer and the overall square patterned resistive sheet structure showing the four basic design parameters: array period *a*, gap distance *d* to the mirror, the side length of square openings *l*, and resistive sheet resistance R_s.

Fig. 4.3 shows the HFSS^{TM} finite-element-method electromagnetic calculated spectral response for the square patterned resistive sheet structure for array period a = 9.3μm and square hole side length l = 3.72μm. R_s is varied from a perfect electric conductor (PEC) to 9Ω/□ while the gap distance d is fixed at 2.5μm. When R_s is zero (i.e., it is a PEC), it should not absorb any power. The HFSS^{TM}-calculated reflection coefficient curve (green dotted-dashed) is, for this case, essentially one, and the corresponding absorption is essentially zero. Figure 4.3 shows that for sheet resistance R_s = 3Ω (black solid) absorption of almost all incident power at the center wavelength of 10μm is achieved. Note that varying the sheet resistance R_s has little effect on the center wavelength of the resonant power absorption. If, however, low sheet resistance (R_s = 1Ω) is selected, absorption is weak. If high sheet resistance (R_s = 9Ω) is selected, absorption is strong. Figure 4.4 illustrates HFSS^{TM} finite-element-method electromagnetic calculated spectral responses of a square patterned resistive structure for fixed array period a = 9.3μm, fixed gap distance d = 2.5μm, and variable length of square slots l. Figure 4.4 shows that a patterned resistive sheet structure with length of square slots l = 3.72μm (blue curve) absorbs almost all incident power at the center wavelength of 10μm when the optimized sheet resistance R_s is 3Ω. The length of square slots l (size of square slot) affects the bandwidth of curve, as expected from the FSS literature [7, 8]. Shown in Figure 4.4 are the spectral responses of square slots with varying lengths, where the sheet resistance for each length was selected to produce maximum peak absorption. For fixed array period of slot (a = 9.3μm), the resonance wavelength shows minimal change as the length is varied. As the length of the slot increases, the bandwidth of the curve increases. To maintain high absorption efficiency a wider slot length also requires a larger sheet resistance to preserve the strong absorption.

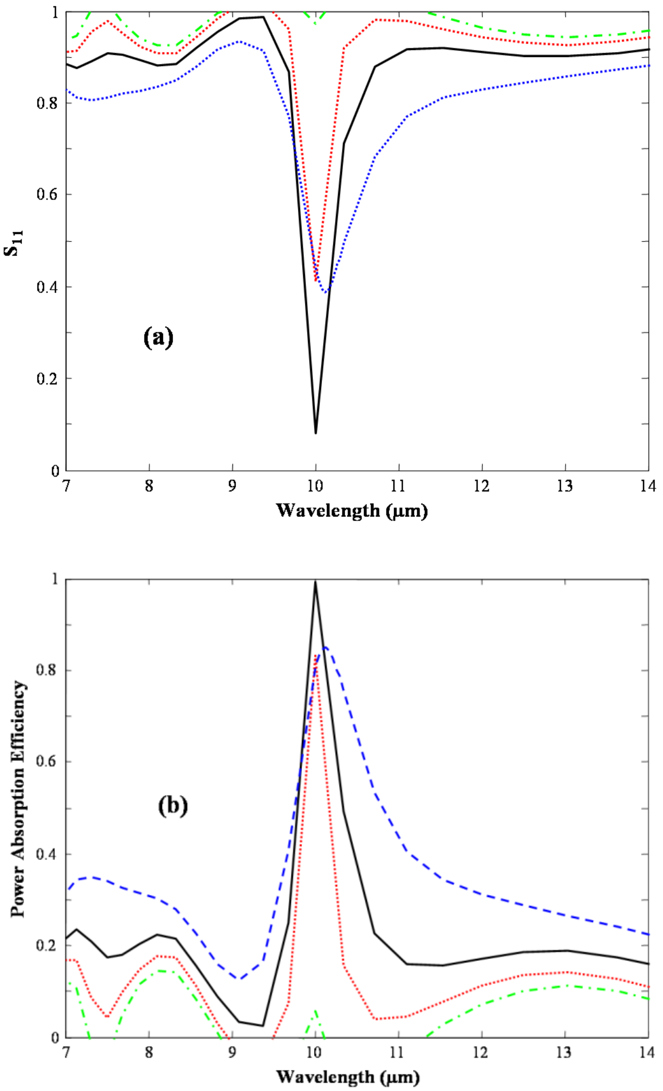

Figure 4.3: Spectral responses as a function of R_s for a square patterned resistive sheet structure for square hole side length l = 3.72μm, array period a = 9.3μm, and thickness of air gap d = 2.5μm: the sheet resistances of the patterned resistive sheet layer is: 0Ω/□ (green dotted-dashed curve), 1Ω/□ (red dotted), 3Ω/□ (black solid), and 9Ω/□ (blue dashed), (a) magnitude of reflection coefficient $|S_{11}|$; (b) power absorption calculated from $1\text{-}S_{11}^2$.

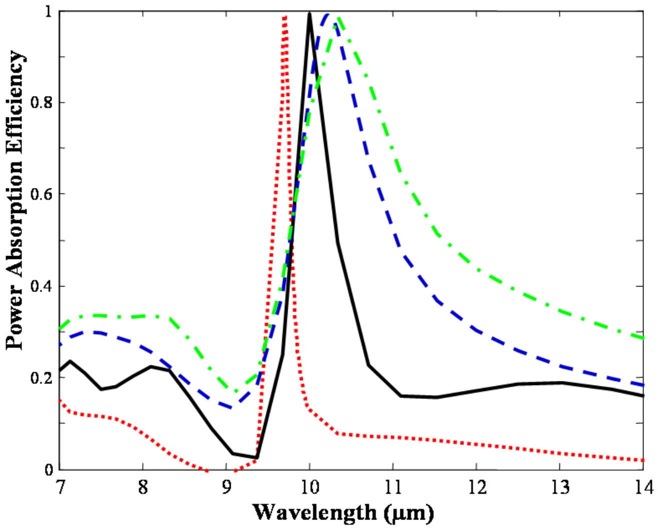

Figure 4.4 Spectral responses due to varying square hole side length *l* with optimized sheet resistance, but fixed array period $a = 9.3\mu m$ and gap distance $d = 2.5\mu m$. Lengths with optimized sheet resistance are: 3.1μm hole in 1Ω/□ sheet (red dotted curve), 3.72μm hole in 3Ω/□ sheet (black solid curve), 4.1μm hole in 7Ω/□ sheet (blue dashed curve), and 4.46μm hole in 9Ω/□ sheet (green dash-dotted curve).

As mentioned in Chapter 3, a cross patterned resistive sheet structure shows a narrowband spectral response with less polarization independent response, especially for 45-degree polarization. Figure 4.5 (a) shows the configuration of square patterned resistive sheet with 45-degree polarization. In Figure 4.5 (b) we see that the absorption spectral responses of the square-patterned resistive sheets are almost identical for TE polarization (black solid curve) and 45-degree polarization.

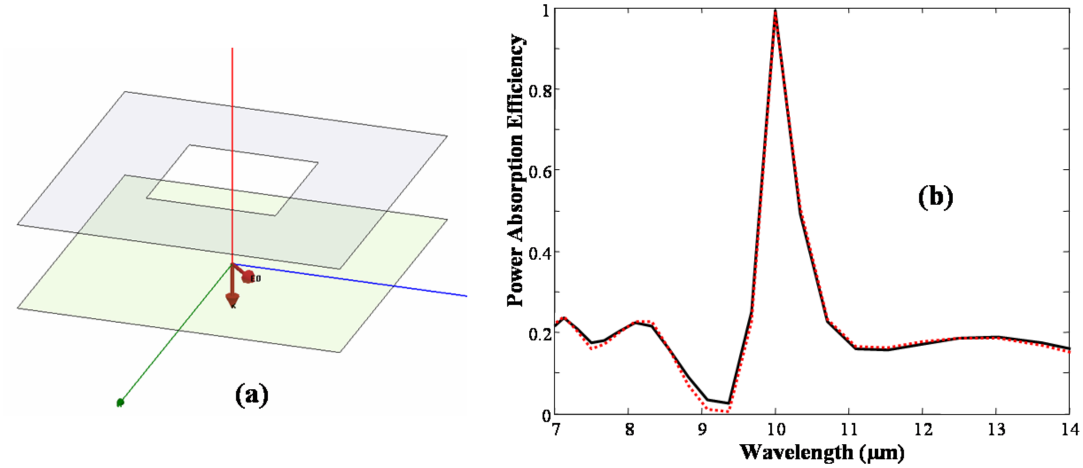

Figure 4.5: (a) Configuration of square patterned resistive sheet structure with 45-degree polarization. (b) Spectral response of square patterned resistive sheet for square hole side length l = 3.72μm, array period a = 9.3μm, thickness of air gap d = 2.5μm, and the sheet resistances of the patterned resistive sheet layer R_s = 3Ω/□; the absorption spectral response of the TM polarization (black solid curve); the absorption spectral response of the 45 degree polarization (red dotted).

4.2 FINITE THICKNESS METAL AS AN ABSORBER LAYER

Design studies have shown that for efficient IR absorption the patterned absorber layer requires a sheet resistance close to 3Ω/□. For realistic, finite thickness metal layers, however, the skin effect produces a complex surface impedance that in the LWIR band can be quite large. Also, the frequency in the LWIR is on the order of the inverse of relaxation time for most metals. Therefore, for accurate modeling we should consider the frequency-dependent AC conductivity of metals. To illustrate we use here the AC conductivity of aluminum (Al) described by the Drude model $\sigma = \sigma_0 / (1 + j\omega\tau)$, assuming a DC conductivity $\sigma_0 = 3.8 \times 10^7$ S/m and relaxation time $\tau = 8.0 \times 10^{-15}$ S [15]. Figure 4.6 presents the HFSS^{TM}-calculated spectral responses for a lossy thin sheet absorber with a sheet resistance of 3Ω/□ (black solid curve) located 2.5 µm in front of a perfect mirror. This is compared to that produced by a finite thickness (30 nm) aluminum absorber layer (red dotted curve) located 2.5 µm in front of an aluminum mirror layer (0.2µm thick). The power absorption for the finite thickness Al metal layer used as the absorber is as good as that found for a thin resistive sheet absorber layer.

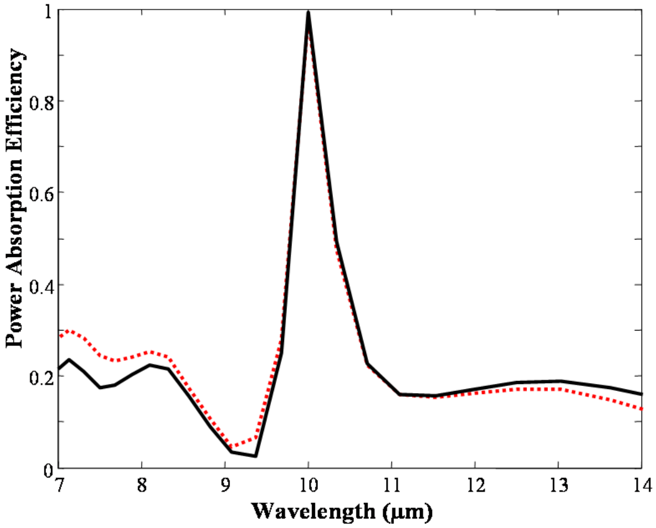

Figure 4.6: Comparison of spectral responses for a thin lossy sheet absorber with sheet resistance 3Ω/□ (black solid curve) and a finite thickness (30 nm) aluminum absorber layer (red dotted curve): array period *a* = 9.3µm, square hole side length *l* = 3.72µm, and gap distance *d* = 2.5µm.

4.3 THREE COLOR DESIGN

In Chapter 3.3 a three-color design was achieved by using a cross patterned resistive sheet structure. Through this same approach, square patterned resistive sheets can achieve three-color focal plane arrays. For the square hole resistive sheet, the center wavelength is set primarily by the size and period of the holes, not the gap between the absorber and the mirror. To demonstrate the possibility of a simpler three-color focal plane array using a square hole patterned resistive sheet, we have applied the constraint that each pixel for each different wavelength uses the same gap thickness d = 2.5µm and the same thickness (30nm) of metal absorber layer. For example, here we selected the center wavelengths of 8, 10, and 12µm. Figure 4.7 shows the HFSS^{TM} calculated spectral responses for a three-color focal plane design. For the fixed ratio of the length and array period (l / a = 0.4), the only differences between the three-pixel designs are the lithographically drawn parameters: the length of square slot l and the array period a, which determines the peak absorption wavelength. Power absorption efficiencies are almost 100% at each center wavelength, with sufficiently narrow bandwidth for a LWIR focal plane array with three non-overlapping colors.

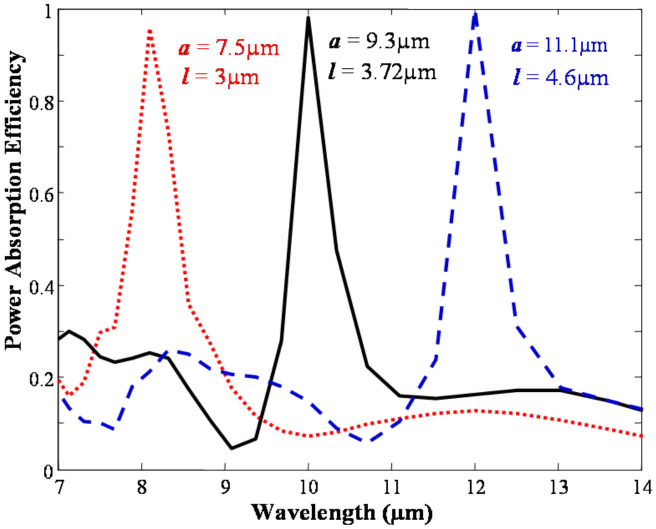

Figure 4.7: Spectral responses for a three-color focal plane design. For the different wavelengths, only the lithographically drawn dimensions of array period *a* and the size of the square hole is varied, with identical gap distance 2.5μm and thickness of Al metal absorber layer 30nm. Array periods with square hole side length are: 7.5μm period with 3μm hole (red dotted curve), 9.3μm period with 3.72μm hole (black solid curve), and 11.1μm period with 4.6μm hole (blue dashed curve).

4.4 DIELECTRIC SUPPORT LAYER

From a fabrication perspective, a square-patterned resistive sheet structure needs to have a dielectric support layer of a certain thickness. In Chapter 3, the cross-patterned resistive sheet structure had a dielectric support layer, with a hole through it. Square-patterned sheet structures also can adopt the same approach as cross patterned sheet structures. Figure 4.8 (a) shows a square-patterned resistive sheet structure that uses a square-patterned hole through both the resistive sheet absorber layer and through a finite thickness (0.3μm) Ge support layer, which is mechanically strong enough to be used as a support layer as mentioned in chapter 2. Figure 4.9 shows calculated spectral responses comparing a structure with the square hole through both resistive sheet absorber layer and dielectric support layer to a structure with only the square patterned resistive absorber layer with no dielectric support layer. Note that if there is no hole through the dielectric support layer, there is a strong dielectric loading effect, as well as interference effects in the dielectric and gap. This causes the center of the resonant wavelength to shift to much longer wavelengths (in this case, out of the LWIR band). Etching holes through the dielectric support layer, however, produces a structure whose effect on the spectral response is much less. The use of patterned holes, whose area is 16%, through the dielectric layer can have the added benefit of reduced thermal mass, thus allowing faster response times. When the structures use the same array period and square slot size, the structure with a hole through both absorber layer and dielectric support layer produces excellent power absorption. The center of the resonant wavelength shifts, however, to a somewhat longer wavelength compared to the structure without dielectric support.

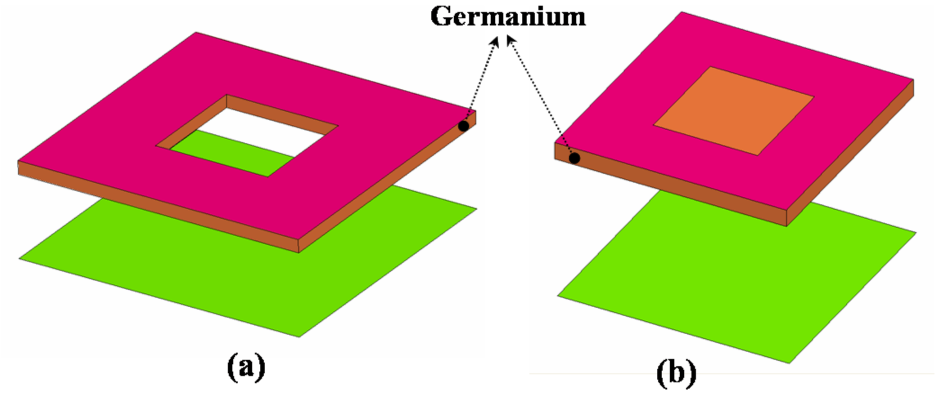

Figure 4.8: (a) configuration of hole in dielectric layer for square patterned resistive sheet structure; (b) configuration of no hole in dielectric layer for square patterned resistive sheet structure.

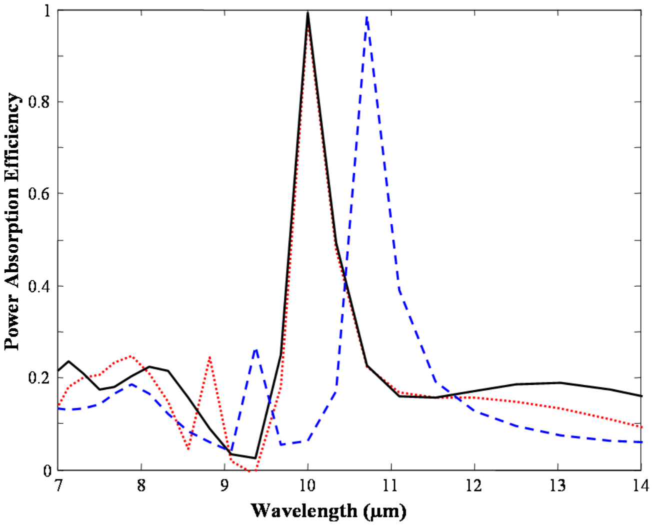

Figure 4.9: Spectral responses with and without dielectric support layer: black solid curve: square patterned resistive sheet structure without dielectric support layer, array period *a* = 9.3μm, square hole side length *l* = 3.72μm, ratio of the length and array period *l* / *a* = 0.4, thickness of gap *d* = 2.5μm, and resistive sheet absorber layer with sheet resistance R_s = 3Ω/□; blue curve (dashes): square patterned resistive sheet structure with hole through both resistive sheet absorber layer and dielectric support layer, array period *a* = 9.3μm, square hole side length *l* = 3.72μm, ratio of the length and array period *l* / *a* = 0.4, thickness of gap *d* = 2.2μm, resistive sheet absorber layer with sheet resistance R_s = 1.5Ω/□, and finite thickness (0.3μm) germanium support layer; red curve (dots): square patterned resistive sheet structure with hole through both resistive sheet absorber layer and dielectric support layer, array period *a* = 8.7μm, square hole side length *l* = 3.48μm, ratio of the length and array period *l* / *a* = 0.4, thickness of gap *d* = 2.2μm, resistive sheet absorber layer with sheet resistance R_s = 1.5Ω/□, and finite thickness (0.3μm) germanium support layer.

To move the resonant wavelength back to wavelength 10μm, we must change the array period from a = 9.3μm to a = 8.7μm. This is necessary because the array period's effective size is larger than that when patterned resistive sheets without dielectric layer.

We should then increase the square hole side length to retain the same sheet resistance $R_s = 3\Omega/\square$; or we should decrease the sheet resistance to keep the ratio of the length and array period l / a = 0.4.

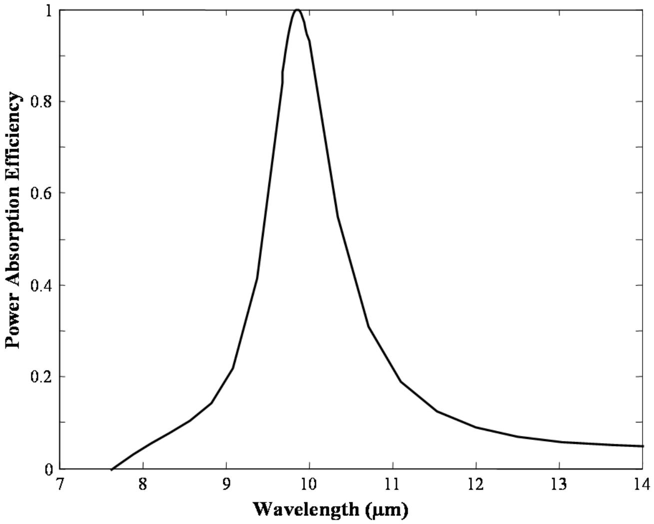

Figure 4.10: Spectral responses for a square patterned resistive sheet structure which has no hole in dielectric layer as shown in Figure 4.8 (b): array period $a = 4\mu m$, square hole side length $l = 1.8\mu m$, ratio of the length and array period $l / a = 0.45$, thickness of gap $d = 2.5\mu m$, resistive sheet absorber layer with sheet resistance $R_s = 1\Omega/\square$, and finite thickness (0.3μm) germanium support layer.

However, since the array period of a square hole patterned resistive sheet determines primarily the resonance wavelength, a sufficient number of periods must be present for the wavelength selective absorption to occur [23, 24]. This in turn will limit the minimum size of the microbolometer pixel. As mentioned above, no hole through the dielectric support layer results in a strong dielectric loading effect, which increases the effective array period. Then to move the resonant wavelength back the size of the array period should be deceased. Then the structure without a hole in the dielectric support layer, as shown in Fig. 4.8 (b), helps reduce the size of microbolometer pixel. Figure 4.10

shows the calculated spectral response for the structure, shown in Fig. 4.8 (b), without a hole in the dielectric support layer. The square patterned resistive sheet structure produces, at a wavelength of nearly 10µm, excellent narrow band absorption even with an array period of a = 4µm.

4.5 CIRCULAR PATTERNED RESISTIVE SHEETS

A circular patterned hole is perfectly independent of polarization. Therefore, to achieve a narrowband spectral response with perfectly polarization independent response, circular-patterned resistive sheet structure, shown in Fig. 4.11, is presented. There are four basic design parameters for circular-patterned resistive sheet structure: array period a, air gap distance d to the mirror, radius of circular hole r, and sheet resistance of the resistive sheet R_s. For circular-patterned resistive sheet structure, the behaviors are similar to the behaviors of square-patterned resistive sheet structure. The resonance wavelength for circular-patterned resistive sheets is set primarily by the size of the array period. Also, as the size of circular hole increases, the bandwidth of absorption curve increases. To maintain high absorption efficiency a bigger size hole also requires a larger sheet resistance to produce strong absorption. Figure 4.12 illustrates HFSS^{TM} calculated spectral responses of circular patterned resistive structure for array period a = 9.3µm, radius of circular pattern hole r = 2.4µm, air gap distance d = 2.5µm, and sheet resistance of the resistive sheet R_s = 4Ω/□. Circular patterned resistive sheets produce excellent narrow band absorption in LWIR band.

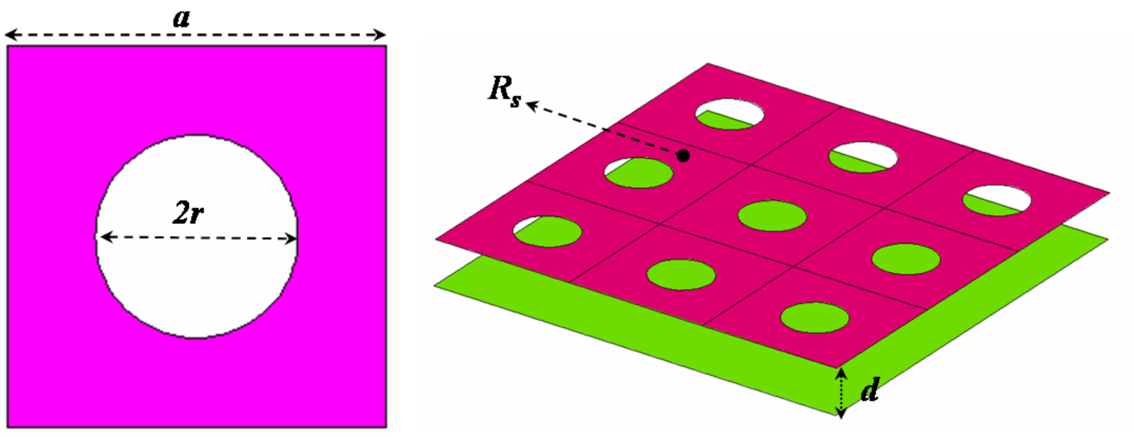

Figure 4.11: Schematic of single unit cell of a circular hole patterned absorber layer and the overall circular patterned resistive sheet structure showing the four basic design parameters: array period *a*; gap distance *d* to the mirror; radius of circular hole *r*; and sheet resistance of the resistive sheet R_s.

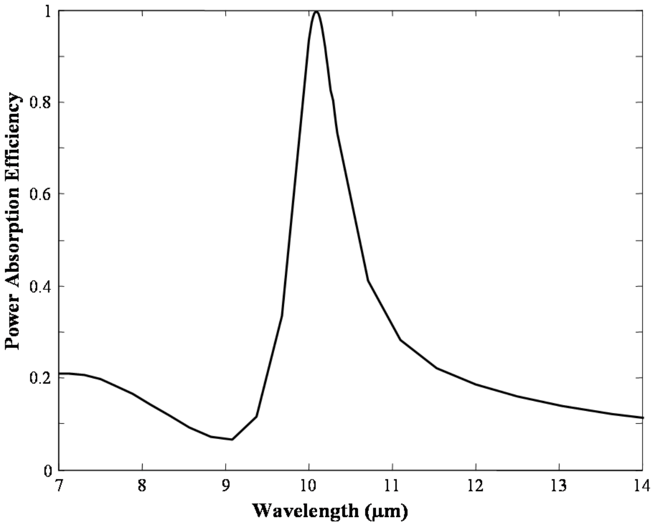

Figure 4.12: Spectral responses for circular patterned resistive sheet structure with array period a = 9.3μm, radius of circular pattern hole r = 2.4μm, air gap distance d = 2.5μm, and sheet resistance of the resistive sheet R_s = 4Ω/□.

4.6 CONCLUSIONS

The design of square and circular hole patterned resistive sheet structure has been theoretically investigated for use in wavelength selective long wave infrared (LWIR) focal planes arrays. Square and circular hole patterned resistive sheet structure produces a narrowband spectral response with a perfect polarized independent response. The cut off wavelength for spectral response is wavelength of array period size, so the resonance wavelength occurs at near wavelength of array period size. As the length of the slot increases, the bandwidth of the curve increases. To maintain high absorption efficiency a wider slot length also requires a larger sheet resistance to preserve the strong absorption. Square hole patterned resistive sheet structures using finite thickness metal layers as the absorber can have high absorption at the designated wavelength and produce enough spectral selectivity to allow a multi-color system spanning the 7-14µm band. However, since the array period of a square hole patterned resistive sheet primarily determines the resonance wavelength a sufficient number periods must be present for the wavelength selective absorption to occur. This in turn will finite limit the minimum size of the microbolometer pixel. Initially simulations suggest at least three array periods are required, corresponding to a minimum pixel size of approximately 28µm for a center wavelength of 10µm.

Chapter 5: Reduced Thermal Mass Infrared Microbolometer

5.1 INTRODUCTION

There are two major ways to detect infrared radiation – photon detection and thermal detection. Photon detectors are able to provide faster response time than thermal detectors [25]. Photon detectors, however, require a cryogenic cooling system. These expensive, bulky, and heavy to use systems prevent thermal generation of charge carriers. In constant photon detection, uncooled infrared thermal detectors such as microbolometers need no cooling system at all. However, the response speed of an infrared microbolometer is slow due to the very high thermal resistances required for sensitive microbolometer performance. The only way to increase the response speed is to reduce the thermal mass, which is proportional to the mass of the absorbing structure. For mechanical support, microbolometers require a finite thickness dielectric support layer; this limits how much we can reduce the thermal mass of the microbolometer. Rather than make thinner dielectric support layers, we can make sub-wavelength-sized patterned holes (square and circular) that reduce the thermal mass with little to no loss in IR absorption efficiency.

5.2 DC ESTIMATE FOR SQUARE PATTERNED RESISTIVE SHEETS

In Chapter 4, we saw that narrow band absorption could be achieved using periodic square or circular patterned resistive sheet structures. We showed that the bandwidth of absorption curve was affected by the size of the patterned hole. The bandwidth of curve increased as the size of the patterned hole increased. To maintain high absorption efficiency a larger hole required a larger sheet resistance.

Drawing on my understanding of this phenomenon, I apply sub-wavelength-sized square or circular holes to reduce the thermal mass of microbolometer. Figure 5.1 shows a schematic of a single unit cell of a square-patterned absorber layer and the overall square-patterned resistive sheet structure. Finding the optimized sheet resistance for certain sized holes is critical, though difficult, to producing broad band absorption. If the size of structure such as a periodic patterned hole is miniscule compared to the wavelength, the sheet resistance of the structure could be approximated by the dc behavior. Figure 5.2 shows the dc sheet resistance approximation of a single unit cell of a square-hole-patterned resistive sheet when array period a is much smaller than the wavelength. The equivalent potential of a sheet with holes causes the current crowding to flow on the sheet as shown in Fig. 5.2 (a). Two possible simple estimates can account for current crowding on a sheet with holes.

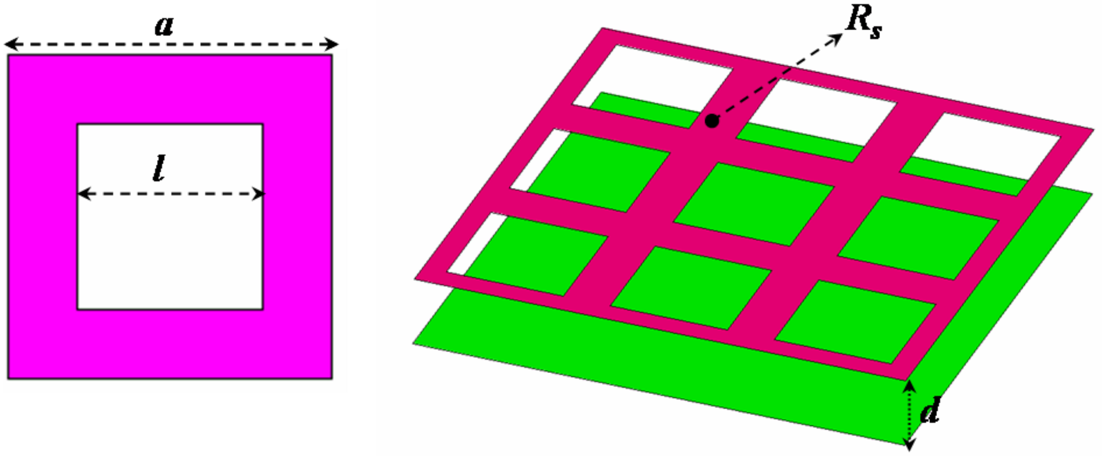

Figure 5.1: Schematic of a single unit cell of a square-hole-patterned absorber layer and the overall square-patterned-resistive sheet structure showing the four basic design parameters: array period *a*; gap distance *d* to the mirror; side length of square openings *l*; and resistive sheet resistance R_s.

One estimate is the lower bound, as shown Fig 5.2 (b), and the other is the upper bound, as shown Fig 5.2 (c). In the case of lower bound, the current flux flows on both ends and two sides of the sheet, therefore the resistive sheet resistance is:

$$R_{lower} = R_s\left(\frac{a-l}{a}+\frac{l}{a-l}\right) \tag{Eq. 5.1}$$

In the case of the upper bound, the current flux flows on just two long sheets. Therefore the resistive sheet resistance is:

$$R_{upper} = R_s\left(\frac{a}{a-l}\right) \tag{Eq. 5.2}$$

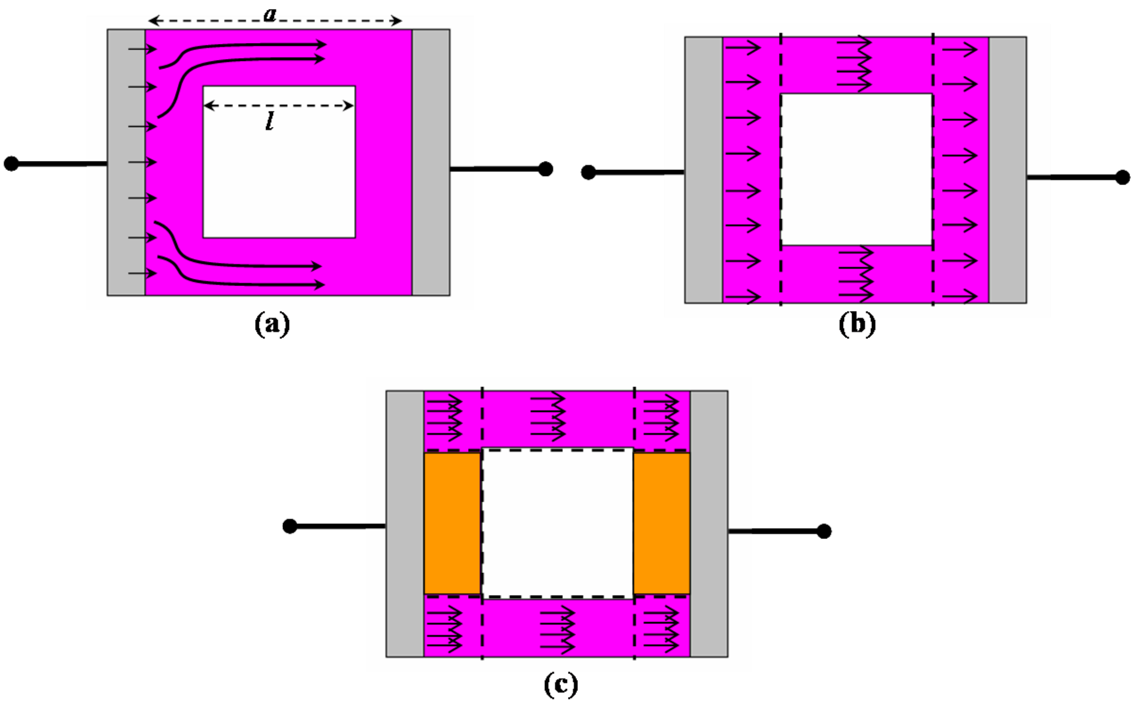

(a)

(b)

(c)

Figure 5.2: Single unit cell of square patterned resistive sheet for DC estimate, (b) lower bound case, and (c) upper bound case.

For example, if I set array period a = 1μm, which is smaller than the wavelength, and the side length of square hole l = 0.708μm, the fill factor of the sheet is reduced by 50% (hole area 50%). When the sheet resistance of the resistive absorber layer for Salisbury Screen is 377Ω/□, it absorbs maximum power efficiency. Therefore, setting R_{lower} and R_{upper} = 377Ω/□ allows estimates for the necessary sheet resistance R_s for the patterned sheet. Then sheet resistance of lower bound is 138.8Ω/□ and sheet resistance of upper bound is 110Ω/□. Figure 5.3 compares HFSS^{TM} calculated reflection coefficient spectral responses for a square-patterned resistive and a simple Salisbury Screen. As expected, the square patterned resistive sheets with R_s = 377Ω/□ (magenta dotted-dotted-dashed) absorb less than the Salisbury Screen does with R_s = 377Ω/□ (red dotted). On the other hand, the square patterned resistive sheets with both sheet resistances of lower bound (green dotted-dashed) and upper bound (blue dashed) absorb as much power as the Salisbury Screen, despite the fill factor being reduced by 50%. To achieve better absorption, the optimized sheet resistance still needs to be adjusted between the lower and upper bounds. The square-patterned resistive sheets with R_s = 120Ω/□ (black solid) absorbs more power than both lower and upper bounds. As we enlarge the square hole of the patterned resistive sheets, the optimized sheet resistance closes to the upper bound estimate. Figure 5.4 shows HFSS^{TM} calculated reflection coefficient spectral responses for square patterned resistive sheets with array period a = 1μm, side length of square hole l = 0.85μm, and air gap thickness d = 2.5μm; it is compared to a simple Salisbury Screen. The absorption spectral response for a patterned resistive sheet with optimized sheet resistance R_s = 60 Ω/□ (black solid), Fig. 5.4, shows that the optimized sheet resistance is close to the sheet resistance R_s = 57 Ω/□ of the upper bound (blue dashed). Even with the fill factor reduced to 27.75% (hole area 72.25%), the square patterned resistive sheets absorb as much power as the Salisbury Screen with R_s = 377Ω/□ (red dotted).

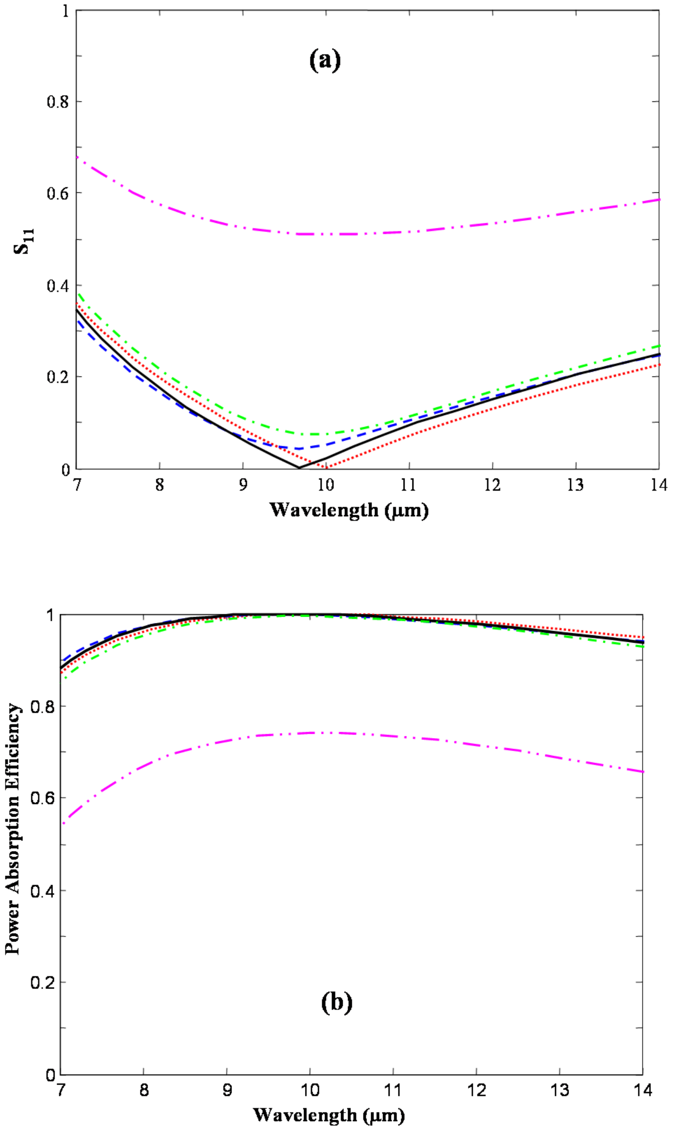

Figure 5.3: A comparison of spectral responses for a simple Salisbury Screen (red curve, dotted) and a square-patterned resistive sheet structure for square hole side length *l* = 0.708μm, array period *a* = 1μm, and thickness of air gap *d* = 2.5μm: the sheet resistances of the patterned resistive sheet layer are: 138.8Ω/□ (lower bound) (green curve, dotted-dashed), 110Ω/□ (upper bound) (blue curve, dashed), 120Ω/□ (black curve, solid), and 377Ω/□ (magenta curve, dotted-dotted-dashed), (a) magnitude of reflection coefficient $|S_{11}|$, and (b) power absorption calculated from $1-S_{11}^2$.

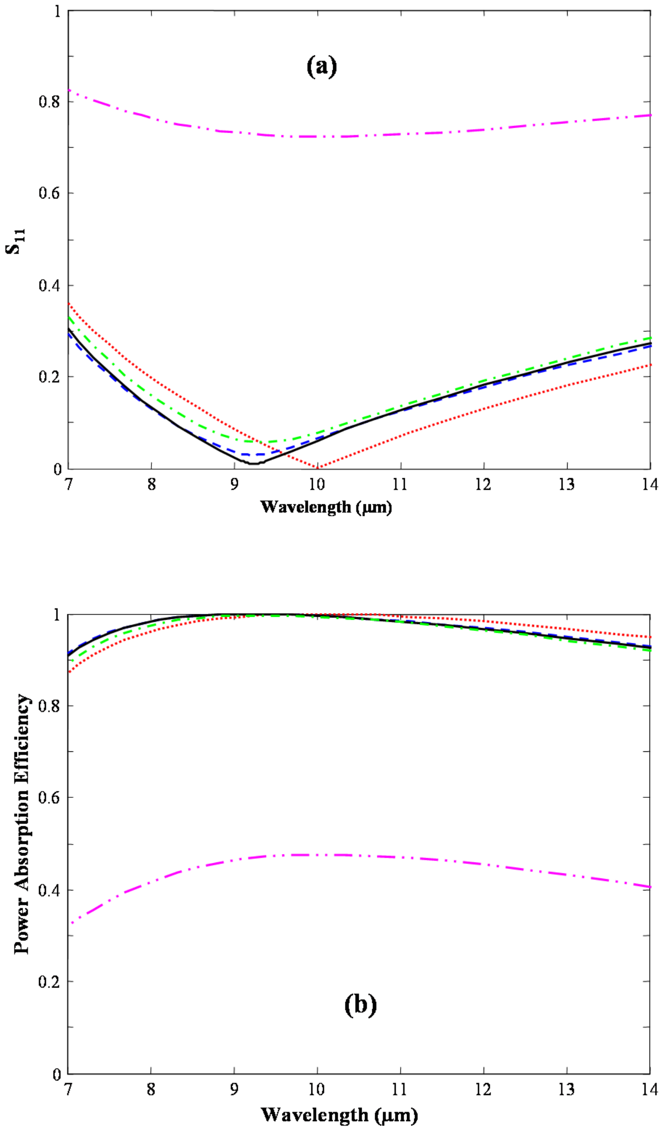

Figure 5.4: Spectral responses compared: a simple Salisbury Screen (red dotted curve) and a square patterned resistive sheet structure for square hole side length *l* = 0.85μm, array period *a* = 1μm, and thickness of air gap *d* = 2.5μm: the sheet resistances of the patterned resistive sheet layer are: 65Ω/□ (lower bound) (green dotted-dashed), 57Ω/□ (upper bound) (blue dashed), 60Ω/□ (black solid), and 377Ω/□ (magenta dotted-dotted-dashed), (a) magnitude of reflection coefficient $|S_{11}|$, and (b) power absorption calculated from $1-S_{11}^2$.

When the array period a is smaller than the wavelength, dc sheet resistance approximation seems a good design approach to finding the optimized sheet resistance for square-patterned resistive sheets. However, fabricating a pattern smaller than 1μm is a difficult process without an electron beam lithography system. Setting the array period a = 5μm makes the square hole side length l to be 3.5μm to keep a 50% fill factor for the patterned resistive sheets. Figure 5.5 shows a HFSS^{TM} calculated spectral response for square hole patterned resistive sheets with array period a = 5μm, side length of square hole l = 3.5μm, and air gap thickness d = 2.5μm; it is compared with a simple Salisbury Screen. The optimized sheet resistance of square patterned resistive sheets with array period a = 5μm and side length of square hole l = 3.5μm is 100Ω/□, which is also close to the sheet resistance R_s = 113Ω/□ of the upper bound estimate. Nevertheless, the square patterned resistive sheets with sheet resistance using both the upper and lower bound estimates absorb nearly the same amount of power as the square patterned resistive sheets with the optimized sheet resistance. As expected, the square patterned resistive sheets with R_s = 377 Ω/□ (green dotted-dashed) absorbs less than the Salisbury Screen with R_s = 377 Ω/□ (red dotted). Also, the Salisbury Screen with R_s = 100Ω/□ (blue dashed) absorbs less than the others.

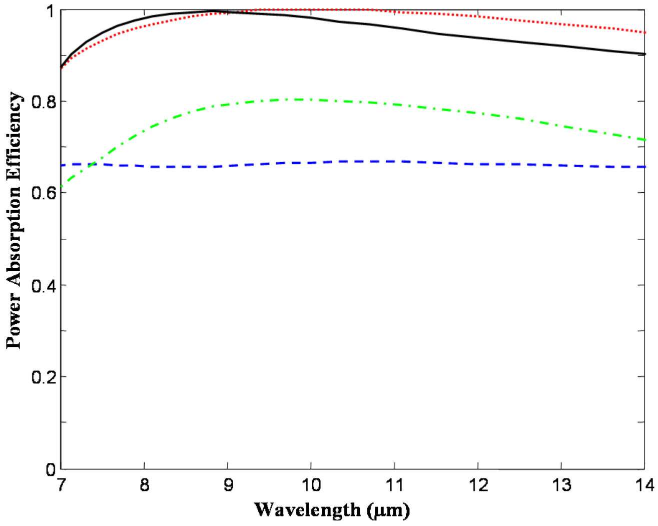

Figure 5.5: A comparison of spectral responses for a Salisbury Screen and a square-patterned resistive sheet structure with square hole side length *l* = 3.5µm, array period *a* = 5µm, and thickness of air gap *d* = 2.5µm: the sheet resistances of the patterned resistive sheet layer is: 100Ω/□ (black solid curve), 377Ω/□ (green dotted-dashed), and the sheet resistances of Salisbury Screen are: 377Ω/□ (red dotted), and 100Ω/□ (blue dashed).

Since LWIR band starts from a wavelength of 7µm, I set the array period to a comparable a = 7µm. Figure 5.6 shows the HFSS^{TM} calculated spectral responses of varying square-hole fill factors, where for each square-hole fill factor the sheet resistance was selected to produce maximum peak absorption. When the square-hole fill factor is 33%, the square-patterned resistive sheets with optimized sheet resistance R_s = 165Ω/□ (blue dashed curve) absorb as much power as the Salisbury Screen with R_s = 377Ω/□ (red dotted). When the square-hole fill factors are 50% (black solid) or 73% (green dotted-dashed), the square-patterned resistive sheets still have good power absorption. However, the square patterned resistive sheets with array periods smaller than wavelength 7µm have better power absorption than the square patterned resistive sheets with array period a = 7µm. If the square hole fill factor surpasses 73%, a finite length of left sheet a – l should, from a fabrication perspective, be considered. When array period a = 1µm and square-hole side length l = 0.85µm are set to keep the square-hole fill factor 72%, the length of left sheet a – l is 0.15µm. This arbitrary finite length of left sheet a – l = 0.15µm allows that the square-patterned resistive sheets with array period a = 7µm have square-hole side length l = 6.85µm (square-hole fill factor 96%). The square patterned resistive sheets with the square-hole fill factor 96% (magenta dotted-dotted-dashed), shown in Fig. 5.6, absorb 50% power in LWIR band.

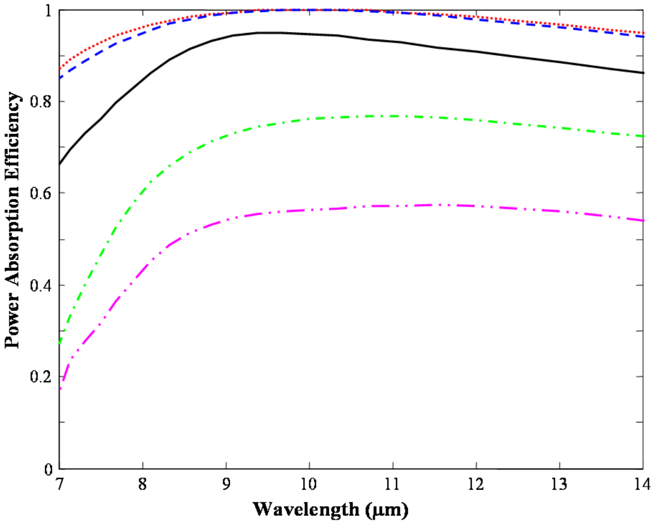

Figure 5.6: A comparison of spectral responses between Salisbury Screen with R_s = 377Ω/□ (red dotted curve) and a square patterned resistive sheet structure with varying square-hole fill factor with optimized sheet resistance, but fixed array period a = 7µm and air gap thickness d = 2.5µm: square-hole fill factors with optimized sheet resistance are: 33% with 165Ω/□ (blue dashed), 50% with 100Ω/□ (black solid), 73% with 80Ω/□ (green dotted-dashed), and 96% with 25Ω/□ (magenta dotted-dotted-dashed).

5.3 DIELECTRIC SUPPORT LAYER

From a fabrication perspective, a patterned resistive sheet structure needs to have a dielectric support layer of certain thickness, which limits how much we can reduce the thermal mass of the microbolometer. Alternatively, we can etch a pattern of holes through the dielectric support layer, shown in Fig. 5.7, to reduce the thermal mass of the microbolometer. As noted above, conventional microbolometers use Si_3N_4 as a dielectric support layer. Also, as we saw in Chapters 3 and 4, germanium support layers are used for patterned resistive sheet structures.

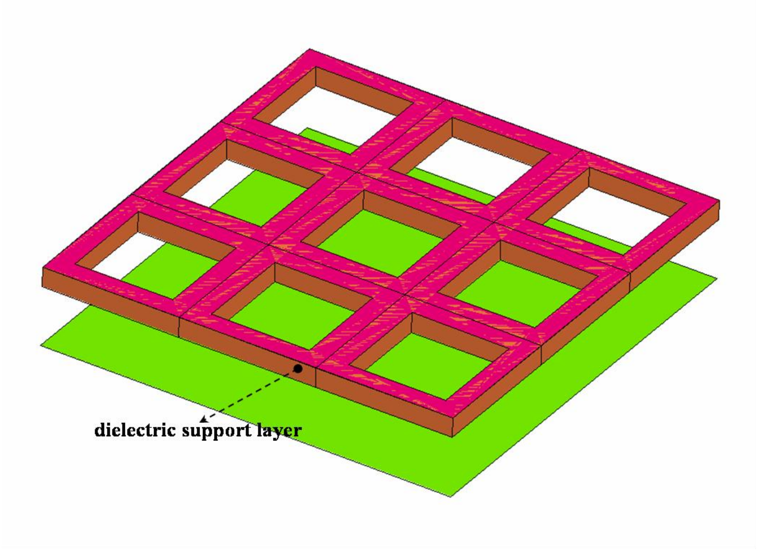

Figure 5.7: Configuration of periodic square-patterned holes in the dielectric layer for square patterned resistive sheet structures.

Figure 5.7 shows a square patterned resistive sheet structure that uses a square patterned hole through both the resistive sheet absorber layer and through a finite thickness (0.3μm) Ge support layer. Figure 5.8 compares a HFSS^{TM} calculated spectral response for a Salisbury Screen with the artificial dielectric support layer and that for square hole patterned resistive sheets with varying air gap thickness d, but fixed array period a, side length of square hole, sheet resistance, and germanium thickness. The square hole patterned resistive sheets with a dielectric support layer for both the square-hole fill factor 50% and 72% produce excellent broad band absorption in the LWIR band. In the case of the 50% square-hole fill factor, the absorption curve of the square-patterned resistive sheets with air gap thickness d = 1.2µm (black solid curve) are almost identical to the absorption curve of the Salisbury Screen with the artificial dielectric support layer whose dielectric constant is 6 (red-dotted curve). The thicknesses of their air gaps and dielectric layers are identical. Therefore, the effective dielectric constant of germanium with square hole is very similar with the dielectric constant of the artificial dialectic layer. Also, in the case of the 72%square-hole fill factor, the effective dielectric constant of germanium with square hole is very similar with the dielectric constant of the artificial dialectic layer, whose dielectric constant is 3. Since array period a is small enough in relation to the wavelength, a good design approach is the approximate estimate of effective dielectric constant. As the array period grows, however, this approximate estimate of effective dielectric constant fails to work. Figure 5.9 shows calculated spectral responses of a structure with the square-shaped hole through both the resistive absorber layer and the dielectric support layer and compares it to a structure with only the square patterned resistive absorber layer with no dielectric support layer. In both the 50% and 73% square-hole fill factor for the square-patterned resistive sheets with array period a = 7µm, a structure with the square-shaped hole through both resistive absorber layer and dielectric support layer has better broadband absorption in the LWIR band than a structure with only the square patterned resistive absorber layer with no dielectric support layer.

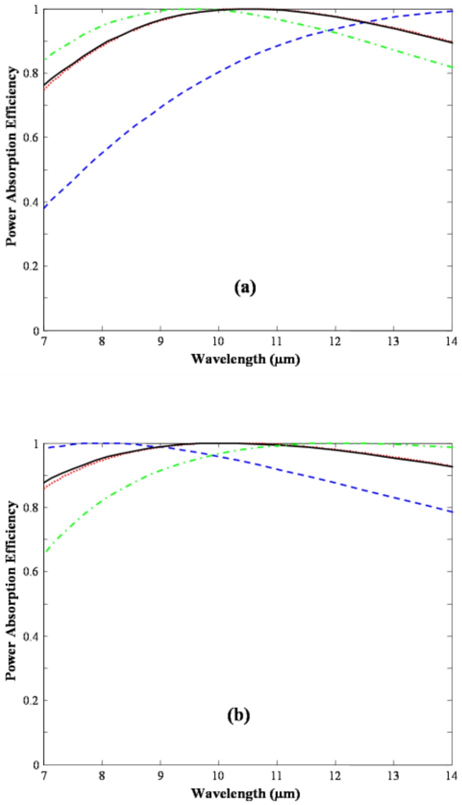

Figure 5.8: (a) Spectral response for a Salisbury Screen with sheet resistance R_s = 377Ω/□, air gap thickness d = 1.2μm, and the thickness of the artificial dielectric layer (dielectric constant = 6) t = 0.3μm (red dotted curve) compared with spectral response for a square-patterned resistive sheet structure with varying air gap thickness d, but fixed array period a = 1μm, side length of square hole l = 0.708μm (the square-hole fill factor 50%), sheet resistance R_s = 120Ω/□, and thickness of germanium t = 0.3μm: air gap thicknesses are: 1μm (green dotted-dashed), 1.2μm (black solid), and 2.2μm (blue dashed); (b) spectral responses for a Salisbury Screen with the sheet resistance R_s = 377Ω/□, air gap thickness d = 1.7μm, and thickness of the artificial dielectric layer (dielectric constant = 3) t = 0.3μm (red dotted curve) compared with that of a square-patterned resistive sheet structure with varying air gap thickness d, but fixed array period a = 1μm, side length of square hole l = 0.85μm (the square-hole fill factor 72%), sheet resistance R_s = 60Ω/□, and thickness of germanium t = 0.3μm: air gap thicknesses are: 1.2μm (blue dashed), 1.7μm (black solid), and 2.2μm (green dotted-dashed).

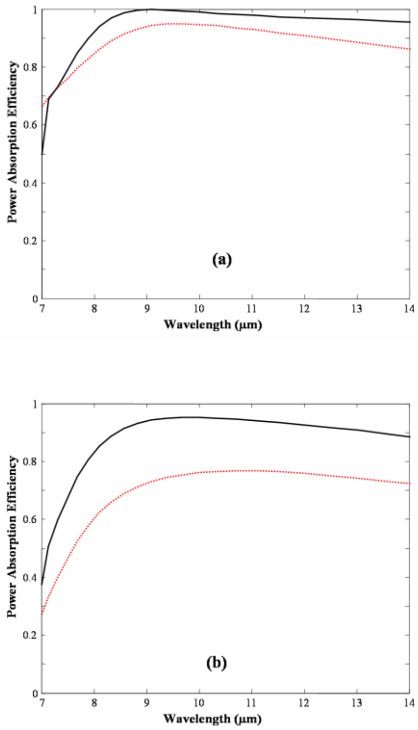

Figure 5.9: (a) Spectral responses with and without dielectric support layer: red-dotted curve: the square patterned resistive sheet structure without dielectric support layer, array period *a* =7µm, side length of square hole *l* = 5µm (the square-hole fill factor 50%), thickness of air gap *d* = 2.5µm,and sheet resistance R_s = 100Ω/□; black solid curve: the square-patterned resistive sheet structure with a hole through both the resistive sheet absorber layer and dielectric support layer, array period *a* = 7µm, side length of square hole *l* = 5µm (the square-hole fill factor 50%), thickness of air gap *d* = 2.2µm, sheet resistance R_s = 100Ω/□, and finite thickness (0.3µm) germanium support layer; (b) spectral responses with and without dielectric support layer: red-dotted curve: the square patterned resistive sheet structure without dielectric support layer, array period *a* =7µm, side length of square hole *l* = 6µm (the square-hole fill factor 73%), thickness of air gap *d* = 2.5µm, and sheet resistance R_s = 80Ω/□; black solid curve: square-patterned resistive sheet structure with a hole through both the resistive sheet absorber layer and dielectric support layer, array period *a* = 7µm, side length of square hole *l* = 6µm (the square-hole fill factor 73%), thickness of air gap *d* = 2.2µm, sheet resistance R_s = 80Ω/□, and finite thickness (0.3µm) germanium support layer.

In Chapter 3, we saw that Si_3N_4 is a bad choice as the dielectric support layer for narrow-band-absorption patterned resistive sheets. Indeed, Si_3N_4 is strongly dispersive in the 8μm to 14μm band []. Si_3N_4, for the broad band application, however, can be good choice. Figure 5.10 shows calculated spectral responses for the square patterned resistive sheets that use a square patterned hole through both the resistive sheet absorber layer and through a finite thickness (0.3μm) Si_3N_4 support layer. The square patterned resistive sheets have, in the LWIR band, excellent power absorption.

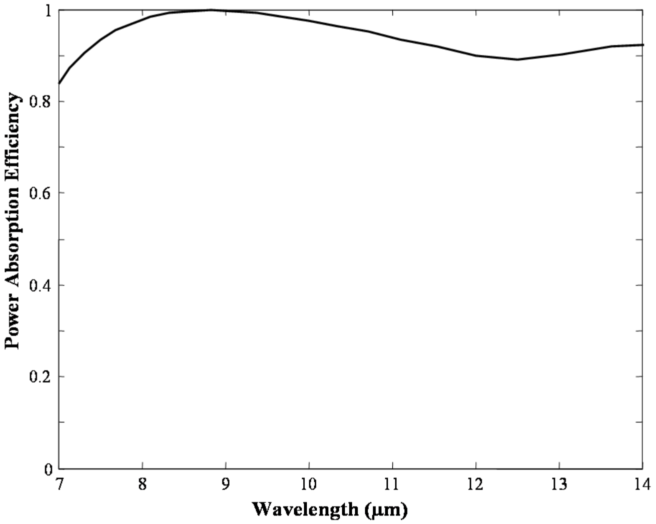

Figure 5.10: Spectral response with the square patterned resistive sheets with array period $a = 5\mu m$, side length of square hole $l = 3.5\mu m$ (square-hole fill factor 50%), air gap thickness $d = 2.2\mu m$, sheet resistance $R_s = 100\Omega/\square$, and finite thickness (0.3μm) Si_3N_4 support layer.

5.4 CIRCULAR PATTERNED RESISTIVE SHEETS

As mentioned in Chapter 4, the spectral response of a circular pattern is perfectly independent of polarization. Also, the circular patterned resistive sheets from Chapter 4 were able to produce, in the LWIR band, narrow band absorption. As the size of circular patterned hole increases, the bandwidth of the absorption curve increases. To maintain high absorption efficiency a larger hole also requires a larger sheet resistance. Figure 5.11 shows a schematic of a single unit cell of a circular patterned absorber layer and the overall circular patterned resistive sheet structure. Figure 5.12 compares a HFSS^{TM} calculated spectral response for a Salisbury Screen with $R_s = 377\Omega/\square$ (red-dotted curve) and circular-hole-patterned resistive sheets with varying circular hole fill factors with optimized sheet resistance, but fixed array period a = 5μm and air gap thickness d = 2.5μm. The circular-patterned resistive sheets with circular hole fill factors of both 50% (r = 2μm) and 72.3% (r = 2.4μm) produce, in the LWIR band, excellent power absorption. Also, the optimized sheet resistance for each circular-hole fill factor of patterned resistive sheets is very close to the optimized sheet resistance for each square-hole fill factor of patterned resistive sheets.

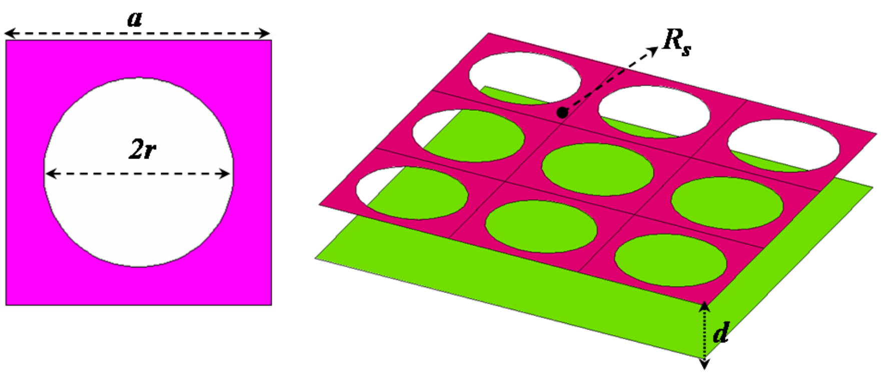

Figure 5.11: Schematic of a single unit cell of a circular patterned hole absorber layer and the overall circular patterned resistive sheet structure, showing the four basic design parameters: array period *a*; gap distance *d* to the mirror; radius of circular hole *r*; and resistive sheet resistance R_s.

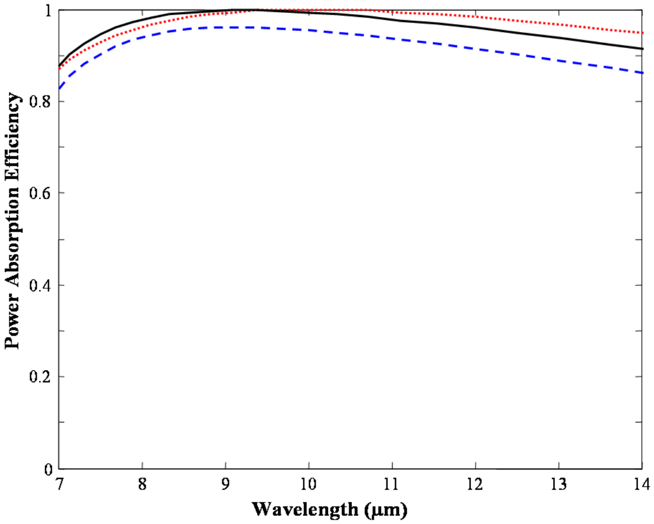

Figure 5.12: A comparison of spectral responses between a Salisbury Screen with R_s = 377Ω/□ (red-dotted curve) and a square-patterned resistive sheet structure with varying square-hole fill factor with optimized sheet resistance, but fixed array period *a* = 5µm and air gap thickness *d* = 2.5µm: square-hole fill factors with optimized sheet resistance are 50% (*r* = 2µm) with 120Ω/□ (black solid) and 72.3% (*r* = 2.4µm) with 60Ω/□ (blue dashed).

5.4 CONCLUSIONS

The design of square and circular patterned resistive sheet structure for IR microbolometers that has substantially reduced thermal mass while maintaining efficient broad band spectral absorption has been discussed. When the array period is smaller than the wavelength, dc sheet resistance approximation seems a good design approach to finding the optimized sheet resistance for square and circular patterned resistive sheets. Even with fill factor of absorber layer reduced to more than 50%, it is possible to absorb as much power as Salisbury Screen by adjusting the sheet resistance in square and circular patterned resistive sheet structure to an optimized sheet resistance.

Chapter 6: Conclusions

These works have presented the method to design the wavelength-selective narrow band absorption using dielectric coated Salisbury Screen and patterned resistive sheet structure. Also, thermal mass reduced microbolometers using periodic patterned holes have been discussed.

In Chapter 2, the measured spectral responses of fabricated modified DSS agree well with plane wave calculation models. The design rules show that the quarter-wavelength dielectric thickness and the half-wavelength air gap thickness with the proper sheet resistance of absorber layer produce excellent tunable narrowband power absorption. The key factor to producing better power absorption is controlling the flatness of dielectric support layer.

In Chapter 3, the design of the cross patterned resistive sheets has been investigated for use in wavelength selective long wave infrared (LWIR) focal planes arrays. Cross patterned resistive sheet structure is less independent of polarization. The absorption curve of the cross patterned resistive sheet with 45-degree polarization shifts slightly to a shorter wavelength. The length of cross slot decides the resonance wavelength, and the width of cross slot affects the bandwidth of absorption curve. As the width of the slot increases, the bandwidth of the curve increases. To maintain high absorption efficiency, a wider slot width also requires a larger sheet resistance to produce strong absorption. Cross patterned resistive sheet structures using finite thickness metal layers as the absorber can have high absorption at the designated wavelength and produce enough spectral selectivity to allow a multi-color system spanning the 7-14 micron band.

In Chapter 4, the design of square and circular hole patterned resistive sheet structure has been theoretically investigated for use in wavelength selective long wave infrared (LWIR) focal planes arrays. Square and circular hole patterned resistive sheet structure produces a narrowband spectral response with a perfect polarized independent response. The cut off wavelength for spectral response is wavelength of array period size, so the resonance wavelength occurs at near wavelength of array period size. As the length of the slot increases, the bandwidth of the curve increases. To maintain high absorption efficiency a wider slot length also requires a larger sheet resistance to preserve the strong absorption. Square hole patterned resistive sheet structures using finite thickness metal layers as the absorber can have high absorption at the designated wavelength and produce enough spectral selectivity to allow a multi-color system spanning the 7-14µm band. However, since the array period of a square hole patterned resistive sheet primarily determines the resonance wavelength a sufficient number periods must be present for the wavelength selective absorption to occur. This in turn will finite limit the minimum size of the microbolometer pixel. Initially simulations suggest at least three array periods are required, corresponding to a minimum pixel size of approximately 28µm for a center wavelength of 10µm.

In Chapter 5, the design of square and circular patterned resistive sheet structure for IR microbolometers that has substantially reduced thermal mass while maintaining efficient broad band spectral absorption has been discussed. When the array period is smaller than the wavelength, dc sheet resistance approximation seems a good design approach to finding the optimized sheet resistance for square and circular patterned resistive sheets. Even with fill factor of absorber layer reduced to more than 50%, it is possible to absorb as much power as Salisbury Screen by adjusting the sheet resistance in square and circular patterned resistive sheet structure to an optimized sheet resistance.

Next step in this work would be to measure and chartreuse finished fabricated devices for square patterned resistive sheet structure as shown in Fig. 6.1. Also, cross patterned resistive sheet structure needs to be fabricated and measured. Since the patterned size of cross is less than 1µm, e-beam lithography system is necessary for cross pattern.

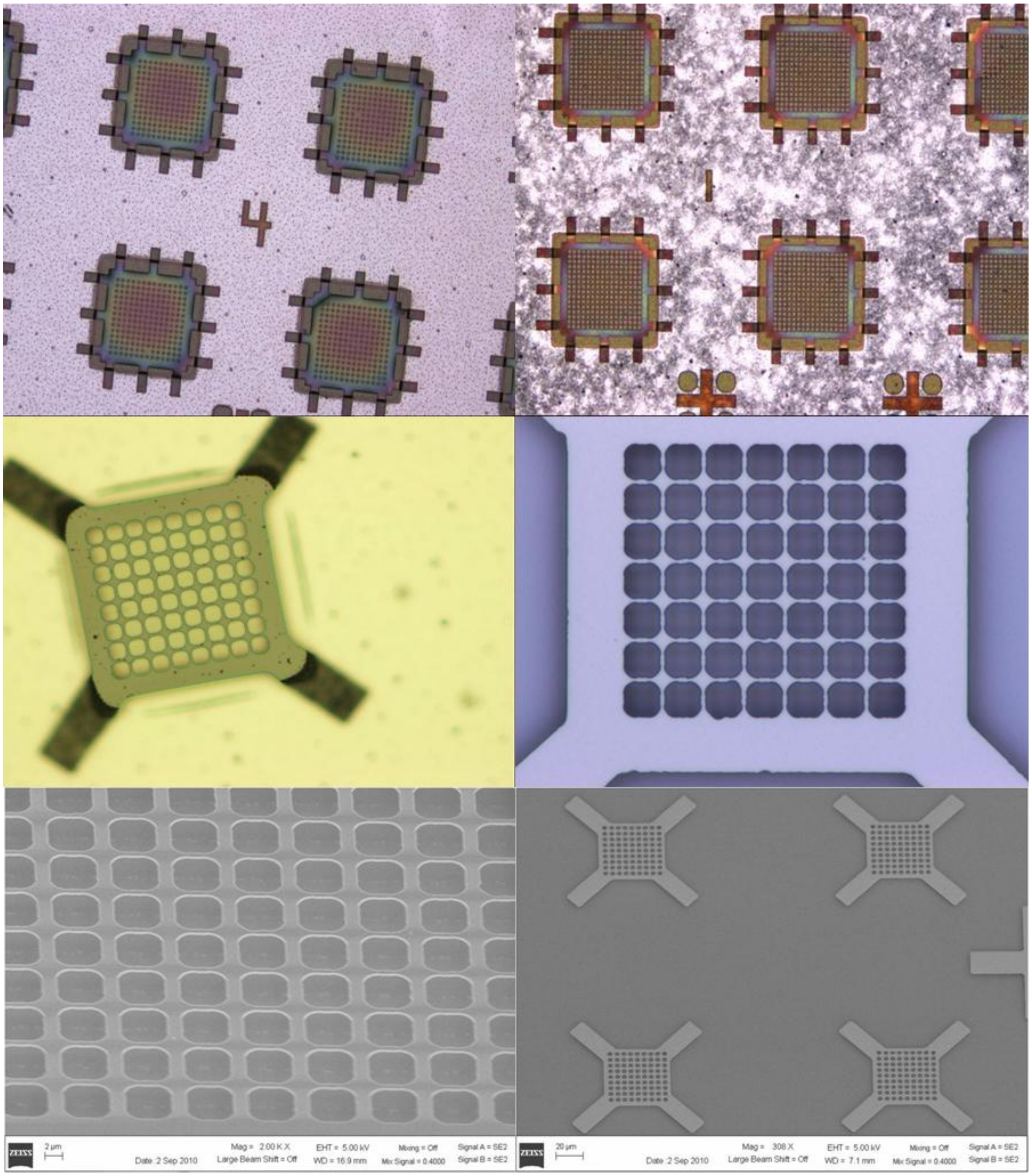

Figure 6.1: Finished fabricated devices for both narrowband and broadband square patterned resistive sheet structure.

References

1. http://www-lep.gsfc.nasa.gov/code693/tdw03/proceedings/docs/session_2/Ngo.pdf
2. R. A. Wood, “Uncooled thermal imaging with monolithic silicon focal planes,” Proc. SPIE, vol. 2020, 1993, pp. 322-329.
3. E. Mottin, A. Bain, P. Castelein, J. L. Ouvrier-buffet, J. L. Tissot, J. J. Yon, J. P. Chatard, “Amorphous silicon technology improvement at CEA/LETI,” Proc. SPIE, vol. 4650, 2002.
4. T. Schimert, J. Brady, T. Fagan, M. Taylor, W. McCardel, and A. J. Syllaios, “Amorphous silicon based large format uncooled FPA microbolometer technology,” Proc. SPIE, Vol. 6940, Iinfrared Technology and Applications XXXIV, 2008, pp. 694023.
5. A. Rogalski, “Reviews of Infrared detectors: status and trends,” *Prog. Quantum Electron*., vol. 27, pp 59-210, 2003.
6. http://themis.asu.edu/zoom-20040806A.html
7. R. Ulrich, “Far-infrared properties of metallic mesh and its complementary structure,” Infrared Phys., vol. 7, 1967, pp37-55.
8. Sakai, K., Fukui, T., Tsunawaki, Y., and Yoshinaga, H., “Metallic mesh bandpass filters and fabry-perot interferometer for the far infrared,” Jpn. J. Appl. Phys., 1969, vol. 8, No. 8, pp. 1046-1055.
9. Ben A. Munk, *Frequency Selective Surfaces: Theory and Design,* (Wiley, 2000).
10. S. T. Chase and R. D. Joseph, “Resonant array bandpass filters for the far infrared,” Appl. Optics vol. 22, 1983, pp. 1775-1779.

11. T. K. Wu, *Frequency Selective Surface and Grid Array*, (Wiley, New York, 1995).

12. N. I. Landy, S. Sajuyigbe, J. J. Mock, D. R. Smith, and W. J. Padilla, "Perfect Metamaterial Absorber," Physical Review Letters, vol. 100, 2008, pp. 207402.

13. T. Maier and H. Bruckl, "Wavelength-tunable microbolometers with metamaterial absorbers," Opt. Lett. Vol. 34, 2009, pp. 3012-3014.

14. Wang, Y., Potter, B.J., and Talghader, J.J., "Coupled absorption filters for thermal detectors," Opt. Lett., 2006, vol. 31, No. 13, pp. 1945-1947.

15. E. D. Palik, *Handbook of Optical Constants of Solids* (Academic, 1985).

16. A. Bagolini, L. Pakula, T. L. M. Scholtes, H. T. M. Pham, P. J. French, and P. M. Sarro, "Polyimide sacrificial layer and novel materials for post-processing surface micromachining," J. Micromech. Microeng., vol. 12, 2002, pp. 385-389.

17. S. W. Han, J. W. Kim, Y. S. Sohn and Dean P. Neikirk, "Design of Infrared Wavelength-Selective Microbolometers Using Planar Multimode Detectors," Electron. Lett., Vol.40, 2004, pp. 1410-1411.

18. J-Y Jung, S. W. Han, D. P. Neikirk, A. S. Weling, J. H. Goldie and P. D. Willson, " Wavelength-selective Infrared Detectors Based on Patterned Resistive Sheets," Proc. SPIE, vol. 6542, 2007, pp. 65421G.

19. R. L. Eisenhart and P. J. Khan, "Theoretical and experimental analysis of a waveguide mounting structure,'' IEEE Trans. Microwave Theory Tech. vol. MTT-19, 1971, pp. 706-719.

20. K. D. Moller, J. B. Warren, J. B. Heaney and C. Kotecki, "Cross-shaped bandpass filters for the near- and mid-infrared wavelength regions," Appl. Optics, vol.35, 1996, pp. 6210-6215.

21. *Ansoft HFSS Reference Manual*, Rel. 10, (Ansoft Corporation, 2005).

22. M. Klanjsek Gunde and M. Macek, “Infrared optical constants and dielectric response functions of silicon nitride and oxynitride films,” Physica Status Solidi (A) Applied Research, vol. 183, no. 2, Feb, 2001, pp. 439-499.
23. Miyamaru, F., and Hangyo, M., “Finite size effect of transmission property for metal hole arrays in subterahertz region,” Appl. Phys. Lett., 2004, vol. 84, No. 15, pp. 2742-2744.
24. M. Beruete, M. Sorolla, I. Campillo, and J. S. Dolado, “Increase of tansmission in cut-off metallic hole arrays,” IEEE Microwave and wireless components letters, vol. 15, no. 2, 2005, pp. 116-118.
25. A. Rogalski, “Reviews of Infrared detectors: status and trends,” *Prog. Quantum Electron.*, vol. 27, pp 59-210, 2003.

Vita

Joo-Yun Jung was born in Busan, S. Korea (Republic of Korea) on September 21, 1976, the son of Chang-Sik Jung and Hyang-Suk Hue. After graduating from Busan Jin High School, Busan, Korea, he attended Texas A&M University, Texas, in 2000. He graduated with a Bachelor's degree in Electrical and Computer Engineering in 2004. In September, 2004, he entered the Graduate School of The University of Texas at Austin. He received the degree of Master of Science in Electrical and Computer Engineering in May of 2007, and was admitted to candidacy in the Doctoral program at the University of Texas at Austin in April 2009. During his stay in the doctoral program, he married Sunju Sohn on July 21, 2007, who is Post Doctoral Fellow at the University of Texas at Austin, Center for Social Work Research.

Permanent address: Busan, Suyoung-Gu, Namchun2-Dong
Samik beach Apt. 307-1101
S. Korea (Republic of Korea)

This dissertation was typed by the author.